

Unlocking Multi-Dimensional Integration with Quantum Adaptive Importance Sampling

Konstantinos Pyretzidis,^a Jorge J. Martínez de Lejarza,^a Germán Rodrigo,^a

^a*Instituto de Física Corpuscular, Universitat de València – Consejo Superior de Investigaciones Científicas, Parc Científic, E-46980 Paterna, Valencia, Spain.*

E-mail: k.pyretzidis@ific.uv.es, jormard@ific.uv.es,
german.rodrigo@csic.es

ABSTRACT: We introduce a quantum algorithm that performs Quantum Adaptive Importance Sampling (QAIS) for Monte Carlo integration of multidimensional functions, targeting in particular the computational challenges of high-energy physics. In this domain, the fundamental ingredients for theoretical predictions such as multiloop Feynman diagrams and the phase-space require evaluating high-dimensional integrals that are computationally demanding due to divergences and complex mathematical structures. The established method of Adaptive Importance Sampling, as implemented in tools like VEGAS, uses a grid-based approach that is iteratively refined in a separable way, per dimension. This separable approach efficiently suppresses the exponentially growing grid-handling computational cost, but also introduces performance drawbacks whenever strong inter-variable correlations are present. To utilize sampling resources more efficiently, QAIS exploits the exponentially large Hilbert space of a Parameterised Quantum Circuit (PQC) to manipulate a non-separable Probability Density Function (PDF) defined on a multidimensional grid. In this setting, entanglement within the PQC captures the correlations and intricacies of the target integrand’s structure. Then, the PQC strategically allocates samples across the multidimensional grid, focusing the samples in the small subspace where the important structures of the target integrand lie, and thus generates very precise integral estimations. As an application, we look at a very sharply peaked loop Feynman integral and at multi-modal benchmark integrals.

Contents

1	Introduction	1
2	Monte Carlo integration, Importance Sampling and VEGAS	3
3	Quantum Adaptive Importance Sampling	6
3.1	Constructing the Grid with a Parametrized Quantum Circuit	6
3.2	Quantum Importance Sampling Statistical Framework	8
3.3	Debiasing Strategy using a Tiling Algorithm	10
3.4	Structure and Optimization of the Parametrized Quantum Circuit	12
3.5	Absence of phantom peaks	14
4	Application of QAIS to Multi-Dimensional Integrals	17
4.1	One-loop pentagon Feynman integral in the Loop-Tree Duality	18
4.2	Multi-peak Benchmark Integrals	22
5	Conclusions and Outlook	24
A	Tiling Algorithm	25

1 Introduction

Perturbative Quantum Field Theory has long been established as the leading method for making precise theoretical predictions of observables at high-energy particle colliders. By systematically expanding in the interaction couplings, scattering amplitudes and differential cross sections at high perturbative orders involve loop and phase-space integrals of increasing dimensionality. As experimental facilities such as the CERN’s Large Hadron Collider (LHC) achieve unprecedented measurement precision, there is a growing demand for equally accurate theoretical calculations to ensure a meaningful comparison between theory and experiment.

Therefore, in the context of particle physics phenomenology, there is an extensive need for more efficient theoretical frameworks and computational strategies. The primary computational bottleneck lies in the numerical integration of the high-dimensional functions that arise from the perturbative expansion. In particular, achieving the sub-percent precision required by modern experiments is challenging, as the required number of integrand evaluations grows rapidly with dimensionality. This computational burden is exacerbated by the presence of integrable but numerically unstable singularities, sharp resonant peaks, and oscillatory regions, all of which require very fine resolution and large samples in localized subdomains, though these regions constitute only a tiny fraction of the total integration space.

These issues make brute-force Monte Carlo (MC) integration computationally prohibitive, and in some cases, entirely impractical, motivating the development of sophisticated variance reduction techniques such as Importance Sampling (IS). The most notable example is the VEGAS [1–3] algorithm, which performs Adaptive Importance Sampling with a hyper-rectangular grid, and has become the common standard. Specifically, VEGAS operates by iteratively adapting a piecewise-constant grid that concentrates samples in regions of high variance, dramatically reducing statistical uncertainties for a given budget of function evaluations. VEGAS and its variants, are assimilated into mainstream libraries (e.g. Cuba [4], MadGraph [5], and Sherpa [6] among others). More recently, integrators based on Machine Learning have emerged [7, 8], as well as VEGAS GPU-based optimizations to reduce runtime [9].

As classical integrators approach their practical limits, attention has shifted towards quantum computing, driven by theoretical advances in the field through quantum algorithms such as Shor’s integer factoring [10], Grover’s unstructured search [11], and the Harrow-Hassidim-Lloyd quantum linear solver [12], as well as advancements in the quantum hardware. Quantum algorithms for MC integration have been developed recently [13–19]. The majority of these approaches exploit the quadratic speedup offered by the fault-tolerant algorithm Quantum Amplitude Estimation (QAE) [20, 21].

In this paper, we leverage one of the key strengths of quantum computers, their ability for sampling from probability distributions. Notably, one of the few demonstrations of quantum supremacy [22], where a quantum device outperforms any classical counterpart, was fundamentally a sampling problem. This experiment highlighted the potential of quantum computers to surpass classical systems in specific tasks. With the current surge of generative modeling as a cornerstone of classical machine learning, and sampling being one of the strongest features of quantum devices, the intersection of these fields has attracted significant attention within the quantum computing community [23–28]. Notable examples include Quantum Generative Adversarial Networks (QGANs) [29–32], Quantum Boltzmann Machines (QBM) [33, 34], and Quantum Circuit Born Machines (QCBMs) [35–39]. Among other applications, quantum generative modeling has shown particular potential across a wide range of problems within High-Energy Physics (HEP) [40–46], alongside other promising quantum machine learning approaches that have also been explored [47–53].

In this context, this paper aims to further expand the growing applications of quantum computing in HEP. Specifically, we present a general-purpose quantum algorithm for high-precision numerical integration of high-dimensional functions, that performs Quantum Adaptive Importance Sampling (QAIS). Working within the constraints of the Noisy Intermediate-Scale Quantum (NISQ) era, we intentionally avoid fully fault-tolerant routines. Instead, we focus on classical Importance Sampling schemes motivated by HEP, which already explore exponentially large domains but suffer from the curse of dimensionality, as reflected in the scaling of the error for certain integrals with increasing dimensionality. Our approach uses a Parametrised Quantum Circuit (PQC) to encode a non-uniform proposal Probability Density Function (PDF) in a grid. We use generative modeling to prepare a favorable state. Then,

we sample from the non-trivial high-dimensional proposal PDF encoded in the PQC, thus harnessing the exponential Hilbert space of a quantum system. This allows us to bypass simplifications and specific modeling in the proposal PDF that exists in classical methods, such as the separable PDF of VEGAS. Finally, we benchmark our method using VEGAS as a reference, while focusing on the accuracy and scalability of the integral estimate, and demonstrating how quantum-generated proposal PDFs offer very robust estimates in high-dimensional integration tasks.

The outline of the paper is the following. In Sec. 2 we review the basic ideas of MC integration, IS and the workflow of the VEGAS algorithm. In Sec. 3, we give a detailed description of the QAIS algorithm, especially focusing on the encoding from the PQC to the PDF, as well as the statistical framework that we developed to efficiently estimate the integral, while considering the subtleties that come with quantum computation. In Sec. 4, we present the integration results obtained with QAIS and make a comparison between the optimal proposal PDFs of QAIS and VEGAS, focusing on the accuracy of the integral estimate. The use cases we considered are a Feynman loop diagram and multi-peaked benchmark integrals. Finally, in Sec. 5, we present the conclusions and the outlook for further improvements.

2 Monte Carlo integration, Importance Sampling and VEGAS

Monte Carlo (MC) integration has long been the most widely accepted method of estimating multi-dimensional integrals. In its most basic formulation, the MC estimation of an integral is obtained by randomly sampling points uniformly across the integration domain and evaluating the integrand at these points. In particular, consider the integral

$$I = \int_{\Omega} f(\mathbf{x}) d\mathbf{x} , \quad (2.1)$$

where \mathbf{x} is a vector in \mathbb{R}^d , $\Omega \subset \mathbb{R}^d$ corresponds to the integration domain, and the function $f : \Omega \rightarrow \mathbb{R}$ is the integrand. By drawing a set of N independent and identically distributed random samples $\{\mathbf{x}_1, \dots, \mathbf{x}_N\}$, one obtains the MC estimator

$$\hat{I}_N^{(\text{MC})} = \frac{|\Omega|}{N} \sum_{i=1}^N f(\mathbf{x}_i) = |\Omega| \langle f \rangle , \quad (2.2)$$

with the corresponding variance of:

$$\left(\hat{\sigma}_N^{(\text{MC})} \right)^2 = \frac{|\Omega|^2}{N-1} \left(\frac{1}{N} \sum_{i=1}^N f(\mathbf{x}_i)^2 - \langle f \rangle^2 \right) . \quad (2.3)$$

In general, the power of this method lies in the fact that it imposes minimal demands on the integrand such as the function does not need to be smooth or analytic, demands that in many practical applications, such as in HEP, are often violated.

Importance Sampling (IS) is a statistical technique used to estimate the value of integrals, especially for complex and high-dimensional functions. The objective of IS is to significantly

reduce the variance of the estimate by sampling from a carefully chosen PDF. In IS, the integral in Eq. (2.1) is reformulated as:

$$I = \int_{\Omega} \frac{f(\mathbf{x})}{q(\mathbf{x})} q(\mathbf{x}) d\mathbf{x} , \quad (2.4)$$

where $q(\mathbf{x})$ is the proposal PDF that is both computationally efficient to sample from and closely resembles $f(\mathbf{x})$. In this setup, and given a set of samples $\{\mathbf{x}_1, \dots, \mathbf{x}_N\}$ drawn from $q(\mathbf{x})$, the MC estimator becomes:

$$\hat{I}_N^{(\text{IS})} = \frac{1}{N} \sum_{i=1}^N \frac{f(\mathbf{x}_i)}{q(\mathbf{x}_i)} . \quad (2.5)$$

The variance of the IS estimator is written as:

$$\left(\hat{\sigma}_N^{(\text{IS})}\right)^2 = \frac{1}{N-1} \left(\frac{1}{N} \sum_{i=1}^N \frac{f(\mathbf{x}_i)^2}{q(\mathbf{x}_i)^2} - \left(\hat{I}_N^{(\text{IS})}\right)^2 \right) . \quad (2.6)$$

The precision of the estimator is highly dependent on the choice of $q(\mathbf{x})$. If there is a large discrepancy between $f(\mathbf{x})$ and $q(\mathbf{x})$, such that $q(\mathbf{x})$ does not adequately capture the behavior of $f(\mathbf{x})$, then this discrepancy will propagate to the overall variance, practically increasing it.

The classical version of VEGAS [1, 3] implements an Adaptive Importance Sampling (AIS) strategy to estimate multi-dimensional integrals. VEGAS reformulates the target integral in Eq. (2.1) as an integral over the unit hypercube,

$$I = \int_{[0,1]^d} J(\mathbf{y}) f(\mathbf{x}(\mathbf{y})) d\mathbf{y} , \quad (2.7)$$

by introducing a change of variables $\mathbf{x} = \mathbf{x}(\mathbf{y})$ with Jacobian $J(\mathbf{y}) = |\partial\mathbf{x}/\partial\mathbf{y}|$, chosen to flatten the peaks of $f(x)$ and thus minimize the MC variance. The points $\{\mathbf{y}_i\}$ are sample points drawn from a d -dimensional uniform PDF in the \mathbf{y} -space, i.e. $[0, 1]^d$, and then are mapped to the original \mathbf{x} -space.

On each dimension, each axis is divided into N_g intervals of varying widths $\{\Delta x_i\}_{i=0}^{N_g-1}$,

$$x_0 = a, \quad x_i = x_{i-1} + \Delta x_{i-1}, \quad x_{N_g} = b, \quad (2.8)$$

and a point from the y -space is mapped to the x -space by

$$x(y) = x_i + \Delta x_i (yN_g - i), \quad i = \lfloor yN_g \rfloor \quad (0 \leq y \leq 1). \quad (2.9)$$

with i being the index of the grid cell, in which the point belongs to. The Jacobian is the step function

$$J(y) = N_g \Delta x_i, \quad (2.10)$$

so that with this transformation, a uniform draw in y -space concentrates samples in regions where the Δx_i are the smallest. Thus, the objective becomes to use finer widths, where $|f(x)|$ is largest.

In d dimensions this mapping is applied independently to every coordinate, giving d one-dimensional grids, each with N_g cells, instead of the N_g^d cells of a full discretization. Because in this setting, the Jacobian factorizes as

$$J(\mathbf{y}) = \prod_{i=1}^d J_i(y_i), \quad (2.11)$$

the induced proposal PDF is separable. This product form of the proposal PDF eliminates the exponential computational cost of sample allocation but also cannot capture correlation between different dimensions, thus in certain cases leads to misallocating samples, creating artificial structures (e.g. phantom peaks) or undersampling high-impact regions. This problem becomes amplified as the integrand dimension increases.

With N samples, the VEGAS estimator is

$$\hat{I}_N^{(\text{VEGAS})} = \frac{1}{N} \sum_{i=1}^N J(\mathbf{y}_i) f(\mathbf{x}(\mathbf{y}_i)), \quad (2.12)$$

whose variance is:

$$\left(\hat{\sigma}_N^{(\text{VEGAS})}\right)^2 = \frac{1}{N-1} \left(\frac{1}{N} \sum_{k=1}^N J^2(\mathbf{y}_k) f^2(\mathbf{x}(\mathbf{y}_k)) - \left(\hat{I}_N^{(\text{VEGAS})}\right)^2 \right). \quad (2.13)$$

To balance this variance VEGAS adapts each one-dimensional grid after every iteration. Let n_i be the number of samples that fall in cell i . The algorithm defines the variable,

$$D_i = \frac{1}{n_i} \sum_{x(y) \in \Delta x_i} J^2(y) f^2(x(y)). \quad (2.14)$$

Next, it smooths and compresses the D_i , to a nonlinear, tunable parameter controlled, smoothed and compressed value derived from its current value, its two neighbours, and the global sum. With the D_i being smoothed and compressed, the algorithm chooses the new cell's boundaries $\{\Delta x'_i\}$, so that each updated bin contains exactly $\bar{D} = \frac{1}{N_g} \sum_{j=0}^{N_g-1} D_j$ thereby forcing each new bin to contribute equally to the total variance. Practically, one starts at the left edge of an axis, accumulates the D_i until the running sum reaches the target \bar{D} , then inserts a new boundary at that point. After setting the new boundary, any excess D_i transfers to the next bin, and continues from left to right until the whole axis is re-discretized. This is done separately, dimension by dimension. In each iteration, new samples are generated, and thus new D_i are used on the updated grid.

Since VEGAS is adaptive, each pass produces an estimate I_j with variance σ_j^2 , and after j adaptations the combined result is

$$\bar{I}_N^{(\text{VEGAS})} = \frac{\sum_j \hat{I}_{N,j}^{(\text{VEGAS})} / \left(\hat{\sigma}_{N,j}^{(\text{VEGAS})}\right)^2}{\sum_j 1 / \left(\hat{\sigma}_{N,j}^{(\text{VEGAS})}\right)^2}, \quad \bar{\sigma}_N^{(\text{VEGAS})} = \left(\sum_j 1 / \left(\hat{\sigma}_{N,j}^{(\text{VEGAS})}\right)^2 \right)^{-1/2}, \quad (2.15)$$

which carries a smaller uncertainty than any single iteration. Because the weights are inverse variances, the best adaptations dominate the average. In this work we compare with the original importance sampling VEGAS as implemented in the standard FORTRAN code [2]. Finally, stratified sampling extensions [3] can further lower errors by exploiting more elaborate statistical techniques but still the general scaling to multi-dimensional integrals suffers from the curse of dimensionality.

3 Quantum Adaptive Importance Sampling

In this section, we introduce Quantum Adaptive Importance Sampling (QAIS), a quantum algorithm that leverages a PQC to perform AIS for numerical integration of multi-dimensional functions. The central objective is to construct a PDF that accurately approximates the target integrand. In classical methods, such as VEGAS, the most computationally expensive step is evaluating the function at N distinct sample points. The aim of QAIS is to reduce the number of function evaluations needed to achieve the desired accuracy, by more efficiently allocating samples in the integration domain. It is crucial to note that this approach takes full advantage of the fact that MC integration demands minimal assumptions on the integrand.

QAIS consists of three main elements, as presented in Fig. 1. The Encoding stage, in which the PDF over the integration domain is discretized and mapped into a PQC. The State Preparation stage consists of adapting the parameters of the PQC to effectively shape the PDF generated by the quantum state to approximate the desired target function. In the third stage, the results from the Z -basis measurements of the optimal PQC are processed using a dedicated statistical framework. The QAIS statistical framework is a modified version of conventional IS, adjusted to the quantum computational framework with the objective of fulfilling the requirements inherent to the efficiency of quantum measurements.

3.1 Constructing the Grid with a Parametrized Quantum Circuit

Our objective is to perform IS for numerical integration using an optimal PDF, which is strategically adapted by a quantum protocol on a grid. The first step in this direction is to define the grid through a quantum state. For an n -qubit system, the underlying Hilbert space, is given by:

$$\mathcal{H} = \underbrace{\mathbb{C}^2 \otimes \mathbb{C}^2 \otimes \dots \otimes \mathbb{C}^2}_{n \otimes} = (\mathbb{C}^2)^{\otimes n} . \quad (3.1)$$

where each qubit is associated with a two-dimensional complex vector space \mathbb{C}^2 . The dimension of the space is 2^n . For a d -dimensional integral, each dimension is encoded using q_i qubits. Hence, the full size of the system is $n = \sum_{i=1}^d q_i$, and the reformulation of the Hilbert space is:

$$\mathcal{H} = (\mathbb{C}^2)^{\otimes n} = \bigotimes_{i=1}^d (\mathbb{C}^2)^{\otimes q_i} . \quad (3.2)$$

The grid's resolution of each dimension is determined by the number of qubits used to represent this dimension. Using more qubits per dimension will reveal finer details of the

Quantum Adaptive Importance Sampling (QAIS)

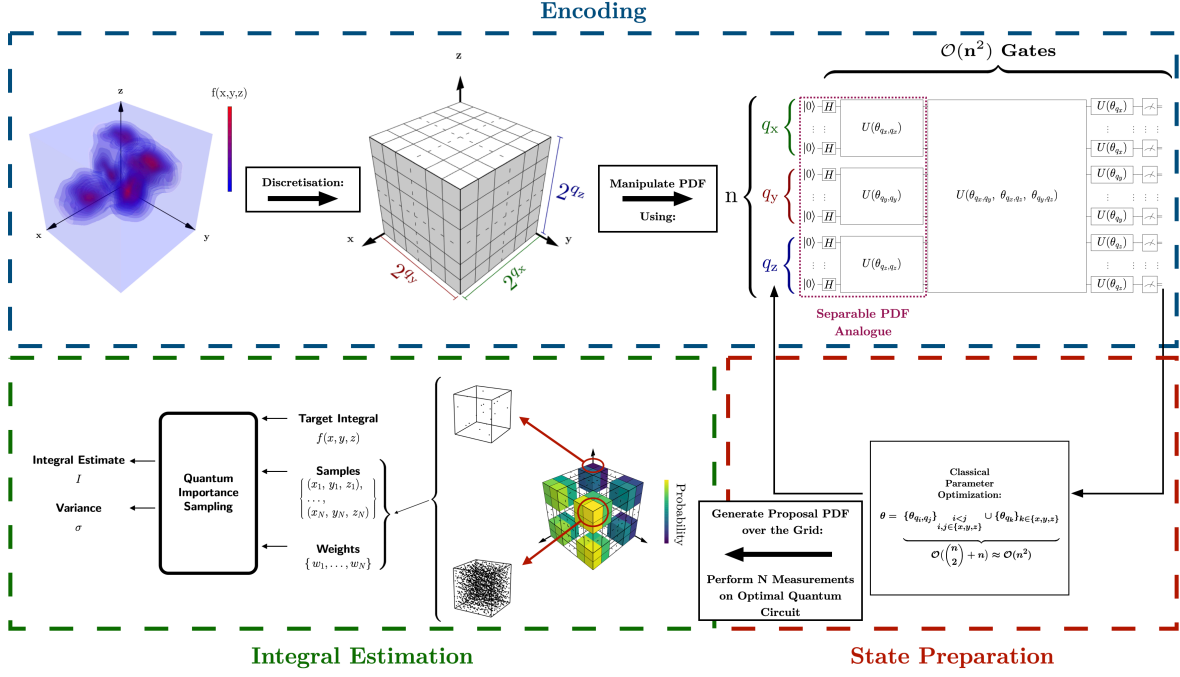


Figure 1. Schematic illustration of QAIS. It consists of three main components: the Encoding, the State Preparation, and the Integral Estimation stages.

integrand structure. The grid coordinates are generated through the Big-Endian Encoding (BEE) scheme. For a d -dimensional domain with integration bounds $\mathbf{a} = (a_1, \dots, a_d)$ and $\mathbf{b} = (b_1, \dots, b_d)$, each dimension i is represented by q_i qubits, corresponding to 2^{q_i} intervals of length

$$\Omega_i = \frac{b_i - a_i}{2^{q_i}} . \quad (3.3)$$

A computational basis state $|j_1\rangle \otimes \dots \otimes |j_d\rangle$ with $j_i \in \{0, \dots, 2^{q_i} - 1\}$ corresponds to and labels the grid cell, with boundaries:

$$\prod_{i=1}^d [a_i + j_i \Omega_i, a_i + (j_i + 1) \Omega_i] . \quad (3.4)$$

For a quantum system, in a general state

$$|\psi\rangle = \sum_{j_1=0}^{2^{q_1}-1} \dots \sum_{j_d=0}^{2^{q_d}-1} c_{(j_1, \dots, j_d)} |j_1\rangle \otimes \dots \otimes |j_d\rangle , \quad (3.5)$$

a Z -basis measurement returns the cell (j_1, \dots, j_d) with probability $|c_{(j_1, \dots, j_d)}|^2$. By interpreting these probabilities as bin heights we construct the piecewise PDF in the continuous space as:

$$q(\mathbf{x}) = \sum_{j_1, \dots, j_d} |c_{(j_1, \dots, j_d)}|^2 \prod_{i=1}^d \frac{1}{\Omega_i} \left[\Theta(x_i - (a_i + j_i \Omega_i)) - \Theta(x_i - (a_i + (j_i + 1) \Omega_i)) \right]. \quad (3.6)$$

Equation (3.6) defines a piecewise-uniform in the integration domain Ω . Because a Z -basis measurement samples exactly one of the 2^n basis states, the shot record $\{k_{(j_1, \dots, j_d)}\}$, follows a multinomial distribution with probabilities $p_{(j_1, \dots, j_d)} = |c_{(j_1, \dots, j_d)}|^2$. For a fixed PQC at N measurements, the maximum-likelihood estimator is simply the empirical frequency, $\hat{p}_{(j_1, \dots, j_d)} = k_{(j_1, \dots, j_d)}/N$. Thus, the BEE construction provides a direct way to construct the full 2^n -cell grid, while the resolution along any dimension can be refined simply by adding qubits to that dimension.

The core novelty of QAIS is the implementation of AIS directly with a PQC. This allows us to operate in a computationally efficient way across the entire Hilbert space $(\mathbb{C}^2)^{\otimes n}$. Through entanglement, quantum gates affect qubits that belong to cross-dimensional parts of the Hilbert space, enabling correlations that go beyond the axis-only separability assumption, thus letting samples to flow from any part of the integration domain to any other. With this approach, we avoid the approximation typically required by the exponential growth of the integration domain's grid size. In particular, we overcome the separability assumption of VEGAS, which intuitively can be thought as restricting to a separable quantum state $|\psi\rangle = |\psi_1\rangle \otimes |\psi_2\rangle \otimes \dots \otimes |\psi_d\rangle$.

Another difference at the encoding level is that QAIS allocates samples by varying the bin heights of the different states through the square amplitudes $|c_{(j_1, \dots, j_d)}^2|$ and increases the resolution by increasing the number of qubits. VEGAS concentrates samples in regions of importance by deforming the grid, while keeping the bin height equal on all of the grid cells.

3.2 Quantum Importance Sampling Statistical Framework

Having defined the PDF on the integration domain through BEE, we are now in a position to construct the statistical framework for performing quantum IS. For this purpose, we clarify how the quantum basis states samples relate to the underlying integration domain. Let Ω be our full discretized integration domain, corresponding to 2^n distinct grid cells. We label these cells as $\{\Omega^{(i)}\}_{i=1}^{2^n}$, where each corresponds to a particular basis-state $|i\rangle$ in the computational Z -basis. Each state $|i\rangle$ is mapped onto a specific, d -dimensional grid interval, according to the notation of Sec. 3.1. Nevertheless, in a linearized setting, the full integration domain is expressed as

$$\Omega = \bigcup_{i=1}^{2^n} \Omega^{(i)}, \quad \Omega^{(i)} \cap \Omega^{(j)} = \emptyset \quad (\forall i \neq j). \quad (3.7)$$

Each grid cell $\Omega^{(i)}$ forms a hyper-rectangle, defined explicitly by intervals determined through the discretization recipe described by Eq. (3.3). Specifically, the grid cell volumes

are given by

$$|\Omega^{(i)}| = \prod_{k=1}^d \Omega_k = \prod_{k=1}^d \frac{b_k - a_k}{2^{q_k}} . \quad (3.8)$$

These volumes are constant for all of the 2^n grid cells, of the integration space, given the equidistant discretization per dimension.

To proceed, we assume state preparation as granted, thus we have a PQC trained to produce a quantum state whose measured PDF approximates the target function of interest in the grid. After sampling from the PQC, we denote with N_i the number of occurrences of the state $|i\rangle$. From a total of N measurements, drawn from the quantum proposal PDF, we obtain N_i samples within each cell $\Omega^{(i)}$. Within each cell, these N_i samples are further distributed to the continuous intervals by generating N_i uniform random points. In our implementation, we draw each cell's samples using quasi-random points, specifically, from a Sobol sequence [54]. This is fully compatible with the discretization and sample allocation by a PQC while it reduces the error further. However, for comparability, we apply and report the standard variance formula. The local integral of the target function $f(\mathbf{x})$ in the cell $|i\rangle$ is

$$I_i = \int_{\Omega^{(i)}} f(\mathbf{x}) d\mathbf{x} . \quad (3.9)$$

Hence, the local MC estimator in $\Omega^{(i)}$ becomes

$$\hat{I}_i = \frac{|\Omega^{(i)}|}{N_i} \sum_{j=1}^{N_i} f(\mathbf{x}_j^{(i)}) , \quad (3.10)$$

where the index i corresponds to the i -th grid cell, and the index j to the j -th random point. Since N_i is the number of times the PQC output fell into cell i , we define the weight of this grid cell as:

$$w^{(i)} = \frac{|\Omega^{(i)}|N}{N_i} . \quad (3.11)$$

Based on these definitions, the total estimator for the integral over Ω is:

$$\hat{I}_N^{(\text{QAIS})} = \frac{1}{N} \sum_{j=1}^N w^{(i)} f(\mathbf{x}_j^{(i)}) . \quad (3.12)$$

The variance of the integral estimate is:

$$\left(\hat{\sigma}_N^{(\text{QAIS})}\right)^2 = \frac{1}{N-1} \left(\frac{1}{N} \sum_{j=1}^N \left[w^{(i)} f(\mathbf{x}_j^{(i)}) \right]^2 - \left(\hat{I}_N^{(\text{QAIS})} \right)^2 \right) . \quad (3.13)$$

While an IS estimator is, in principle, unbiased, there is a subtle but crucial consideration in practice that becomes highly relevant within a quantum computational setting. For quantum computing to offer a meaningful advantage, it is essential that the PQC focuses sampling

on a small subset of the entire 2^n -dimensional Hilbert space specifically those subdomains that contribute significantly to the integral. Typically, integrals over high-dimensional spaces are dominated by a relatively limited region of fluctuating behavior or sharp peaks, while most of the integration domain contributes smoothly or negligibly. This behavior is precisely what motivates the use of IS in a quantum computational framework, since it exactly aligns with the constraints and objectives of both the statistical and the quantum computational setting. However, this advantage also implies that a portion of the integration domain associated to rarely or never observed computational basis states will be overlooked. These regions remain unobserved not because their contribution is strictly zero, but rather because their probability, as defined through the PQC, is too small to produce occurrences in the finite number of quantum measurements performed.

Formally, the estimator of Eq. (3.12) can be re-expressed as:

$$\hat{I}_N^{(\text{QAIS})} = \frac{1}{N} \sum_{i=1}^{2^n} w^{(i)} \sum_{j=1}^{N_i} f(\mathbf{x}_j^{(i)}) = \sum_{i=1}^{2^n} I_i . \quad (3.14)$$

After performing N measurements, we observe a subset of the Hilbert space elements or grid cells, $\Omega^- \subset \Omega$. The remaining states (or grid cells), $\Omega \setminus \Omega^-$, are effectively unseen. The missing mass contribution from $\Omega \setminus \Omega^-$ introduces a bias to the integral estimation, leading to a consistent underestimation. This bias can be explicitly evaluated as

$$\text{bias} = \mathbb{E} \left[\hat{I}_{\text{obs}} \right] - I = - \sum_{i \in \Omega \setminus \Omega^-} I_i < 0 , \quad (3.15)$$

where I is the true integral over the complete domain Ω and \hat{I}_{obs} is the estimator of the integral, based solely on the observed outcomes from performing N measurements on the PQC.

3.3 Debiasing Strategy using a Tiling Algorithm

To quantify and correct this bias, we conceptually partition the integration domain into three regions:

- The **Important Region** $\Omega_I \subset \Omega^-$, containing basis states with significant integrand values and high sampling probability.
- The **Boundary Region** $\Omega_B \subset \Omega^-$, containing adjacent states that surround the Important Region.
- The **Noise Region** $\Omega_N \subset \Omega^-$, consisting of states that are sporadically observed and vary, as a set, across different measurement runs due to shot noise. These states contain low but non-zero probability and appear in isolation, without adjacent measured states.

The union of these regions is $\Omega^- = \Omega_I \cup \Omega_B \cup \Omega_N$. For M measured states after N quantum measurements, the separation defined above identifies the N_I states belonging to the core of

the Important Region and the $N_{B \cup N} = N_B + N_N$ states in the Boundary and Noise Regions, respectively, such that $M = N_I + N_{B \cup N}$.

Our strategy to correct the bias introduced by the unobserved states is to assume that the observed Boundary and Noise Regions are representative samples from the otherwise unobserved region $\Omega \setminus \Omega^-$. Essentially, we build a representative approximation for what we call the non-Important Region $\Omega_{N-I} = (\Omega \setminus \Omega^-) \cup \Omega_B \cup \Omega_N$ and thus reconstruct the PDF in the whole integration domain Ω . Due to our pre-training assumptions, we expect that a very precise sampling of the non-Important Region is unnecessary, as their overall contribution to the integral and consequently the corresponding uncertainty are minor. Additionally, our main focus is to construct the non-Important Regions computationally efficiently, rather than generating a very detailed representation of the substructures that exist within them.

In practice, for each of the $N_{B \cup N}$ cells in the Boundary and Noise Regions, we construct an enlarged hyper-rectangular domain $\{\tilde{\Omega}^{(k)}\}_{k=1}^{N_{B \cup N}}$. Each enlarged domain $\tilde{\Omega}^{(k)}$ contains exactly one measured boundary or noise cell along with its adjacent unobserved states, ensuring a one-to-one correspondence with $\Omega_B \cup \Omega_N$, and a number of hyper-rectangles bounded from above by M . The previously missing integral contribution associated with the unobserved cells, is explicitly taken into account by the redistribution of samples from $\Omega_B \cup \Omega_N$ to these enlarged sub-domains, while ensuring no extra sampling is required. The integral estimator, in this corrected setup is:

$$\tilde{I} = \sum_{i \in \Omega_I} w^{(i)} \sum_{j=1}^{N_i} f(\mathbf{x}_j^{(i)}) + \sum_{k \in \Omega_{N-I}} \tilde{w}^{(k)} \sum_{j=1}^{\tilde{N}_k} f(\mathbf{x}_j^{(k)}), \quad (3.16)$$

where the adjusted weights $\tilde{w}^{(k)}$ take into account the shapes of the new enlarged hyper-rectangular domains and \tilde{N}_k refers to the number of random samples drawn within each enlarged domain $\tilde{\Omega}_k$. Through this construction, we explicitly include all previously neglected states, eliminating missing regions and ensuring that the estimator is unbiased.

In practice, for constructing the non-Important Region, we employ a Tiling algorithm. This algorithm generates a small number of contiguous, non-overlapping hyper-rectangles that collectively cover every previously unobserved grid cell, a process that corresponds to a full tiling of the d -dimensional integration domain. For the construction of such an algorithm, it is important to have a computational cost that scales polynomially with the number of observed states M , the dimension of the integration space d , and the number of qubits used for discretization n . It is an explicit and crucial constraint for the Tiling algorithm not to scale with the number of unobserved, Non-Important grid cells, since, in this framework, this is an exponential sized quantity.

The Tiling algorithm we compose is based on the delta encoding [55, 56]. We compress each contiguous block of unmeasured outcomes between two observed states into a single gap, storing by it by its length and it's lower binary boundary so that we can later sample uniformly within it. To cover the full integration space, these gap records are converted into

hyper-rectangle intervals by a routine similar to the greedy-meshing heuristic well known in computer graphics [57] and generalized here to arbitrary d -dimensional grids.

The details of the Tiling algorithm can be found in Appendix A. The procedure works by generating greedy expansions between blocks of different dimensions. By leveraging this approach, the algorithm skips large blocks of lower-ordered dimensions, when making expansions in a higher ordered dimension. In this way, it efficiently tiles arbitrarily sized gaps in the d -dimensional grid with hyper-rectangles, using at most $2(d - 1) + 1$ intervals per gap. This bound on the number of intervals is the key factor behind the suitable scaling of the Tiling algorithm. After accounting for all operations, even the arithmetic operations, the tile generation executes in time $\mathcal{O}(M d^3 n^2)$. This, compared to the state-sorting cost $\mathcal{O}(n M \log M)$, is typically negligible. Therefore, the asymptotic overhead coming from the tiling procedure is essentially $\mathcal{O}(M \log M)$.

3.4 Structure and Optimization of the Parametrized Quantum Circuit

In order to perform state preparation, we employ a QCBM to train the PQC of the proposal PDF. The target function $f(\mathbf{x})$ is generally defined over a continuous space and is discretized along with the integration domain into a grid, as discussed in Sec. 3.1. For training, we use the Kullback-Leibler (KL) divergence [58] as a cost function to measure and minimize the distance between the target distribution and the proposal PDF.

We use a discretized version of the KL divergence, which is defined as:

$$D_{\text{KL}}(P\|Q) = \sum_{i=1}^M P(\Omega^{(i)}) \log \left(\frac{P(\Omega^{(i)})}{Q(\Omega^{(i)})} \right), \quad (3.17)$$

where $P(\Omega^{(i)})$ denotes the probability corresponding to the target distribution at a single grid cell $\Omega^{(i)}$ (or state $|i\rangle$) and $Q(\Omega^{(i)})$ denotes the probability of the proposal distribution at the grid cell to which $\Omega^{(i)}$ belongs.

To convert the continuous function f , into a discrete PDF or a Probability Mass Function (PMF) suitable for computing the discretized KL-Divergence, we proceed as follows. We first compute the function at N_i representative points $\{\mathbf{x}_i\}$ within each observed grid cell $\Omega^{(i)}$, accounting in total to $N = \sum_{i=1}^M N_i$ function evaluations. Because the grid is uniform, every cell has the same volume, so common factors cancel in the normalization. Therefore, we construct the PMF by taking the simplified expressions, using $P(\Omega^{(i)}) = f(\Omega^{(i)})/Z$ which is the probability of each grid cell, where $f(\Omega^{(i)}) = 1/N_i \sum_{i=1}^{N_i} f(\mathbf{x}_i)$ is the within-cell function's average and $Z = \sum_{i=1}^M f(\Omega^{(i)})$ the normalization constant. Ideally, for a better precision in the target PMF, the cell-wise sample count, N_i would be updated after each run, by assigning more sample to high probability cells. This, combined with the monitoring of the within-cell variance in high impact region, can provide a criterion that indicates whether the grid resolution must be increased by adding more qubits. However, in this work, for robustness and simplicity, we use a fixed N_i per cell and cache all evaluations, while pre-defining the grid's size.

In a shot-based optimization, a proven strategy [28] is to adopt an implicit cost function such as the Maximum Mean Discrepancy (MMD) with a carefully chosen, qubit-scaling Gaussian kernel, to avoid shot-induced barren-plateaus. However, in this work, rather than focusing on the intricacies of the training or optimization procedures, which are themselves very active areas of research in quantum machine learning (QML) and quantum optimization [59–61], we concentrate on whether the PQC architecture can express the complexities of the target integral’s structure, therefore providing a suitable proposal PDF for IS. To that end, we assume ideal training conditions to carry out state preparation. By using a statevector simulator, we have exact access to all probabilities. Consequently, we can employ the KL divergence without encountering shot-induced trainability issues.

We proceed to introduce the architecture of the PQC used for the training. We employ an all-to-all connectivity approach that contains two-qubit gates and single qubit gates. Each two-qubit gate carries a tunable parameter, and the combination with the single qubit gates defines one layer. The form of the unitary operators are:

$$U^{(k)}(\{\theta_{ij}\}) = \prod_{i < j} e^{-i\theta_{ij}\sigma_i^{(k)}\sigma_j^{(k)}}, \quad U_3(\alpha_l, \beta_l, \gamma_l) \propto e^{-i\beta_l\sigma_l^{(Z)}} e^{-i\alpha_l\sigma_l^{(Y)}} e^{-i\gamma_l\sigma_l^{(Z)}}, \quad (3.18)$$

where the first product runs over all distinct pairs of qubits and k labels a distinct Pauli operator with $k \in \{X, Y, Z\}$. The total number of parameters per layer is $n(n-1)/2 + 3n \sim \mathcal{O}(n^2)$, where n is the number of qubits. The architecture of the PQC is illustrated in Fig. 2.

It is important to note that our main approach employs a highly-expressive multi-parameterized all-to-all connectivity Ansatz. For comparison, we also experimented with the popular Hardware Efficient Ansatz (HEA) [62, 63], testing both its two-qubit CNOT gate version and its two-qubit parameterized gate version with its typical restricted nearest-neighbour connectivity. Based on our experiments, HEA performs significantly worse in this setting, not only for shallower PQCs but also when additional layers are added to match the number of parameters of our proposed Ansatz. Even then, its best cost function value would be substantially behind our proposed Ansatz.

For optimization, we will mainly present results using COBYLA [64, 65]. We have also experimented with other gradient-free methods and the parameter-shift rule combined with ADAM [66], with all methods yielding similar outcomes. However, we did encounter trainability challenges. While training, increasing the number of qubits resulted in slower training and a substantial increase in the number of iterations required to reach a specified D_{KL} . We believe these challenges, are influenced to a certain extent by barren plateaus. Furthermore, the dimensionality of the integration domain and the sharpness of peaks exacerbates these difficulties, suggesting that generating nontrivial PDFs becomes inherently more complex as the number of dimensions increases. Nevertheless, by using sufficient training iterations ($\mathcal{O}(10^4)$), we produced high-quality PDFs. This allowed us to make meaningful comparisons between QAIS and VEGAS in the IS frontier. The following analysis details our findings.

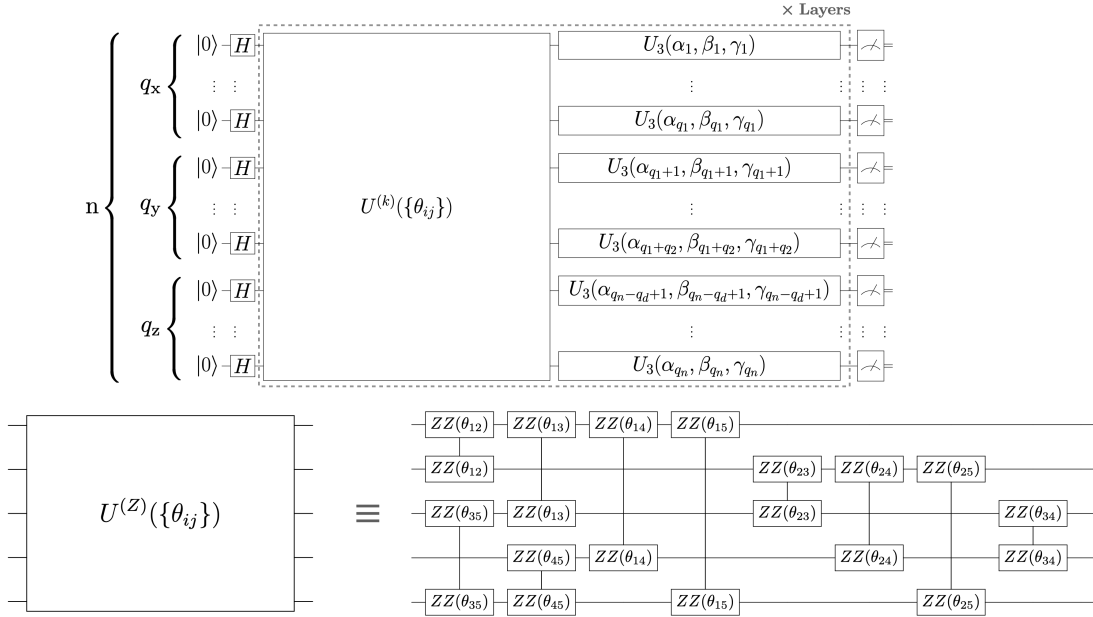


Figure 2. Quantum Circuit architecture used for training. The figure features the general structure with the layer definition (top) as well as an explicit 5 qubit example (bottom).

3.5 Absence of phantom peaks

For a practical demonstration of the complete framework and the differences between QAIS and VEGAS, we present a two-dimensional toy integral composed of two Gaussian peaks in the diagonal. The integral is chosen for its simplicity, while still exhibiting nontrivial features for testing and illustrating the difference between the two methods. Specifically, we define:

$$\int_{[0,0]}^{[1,1]} f(\mathbf{x}) d\mathbf{x} = \int_{[0,0]}^{[1,1]} \left(\sum_{i=0}^1 e^{(-200|\mathbf{x}-\mathbf{r}_i|^2)} \right) d\mathbf{x}, \quad (3.19)$$

where $\mathbf{r}_0 = (0.23, 0.23)$ and $\mathbf{r}_1 = (0.74, 0.74)$. Because the integral can be computed in closed form, it provides a clear benchmark for validating numerical methods. A normalization constant is chosen via analytical integration, so that the integral evaluates to 1.

For QAIS, we have successfully trained a 10-qubit PQC to approximate the shape of $f(\mathbf{x})$ in Eq. (3.19). The Fig. 3 clearly illustrates the distinction between Important and non-Important Regions, since the target function contains large flat regions that contribute minimally, and it highlights differences of the two approaches. VEGAS relies on a strategy whose adaptation mechanism is based on manipulating grid boundaries, and does so separately for each dimension. In contrast, QAIS utilizes a stable grid, with equally spaced grid cells within each dimension. The most crucial difference between the two methods is that QAIS encodes

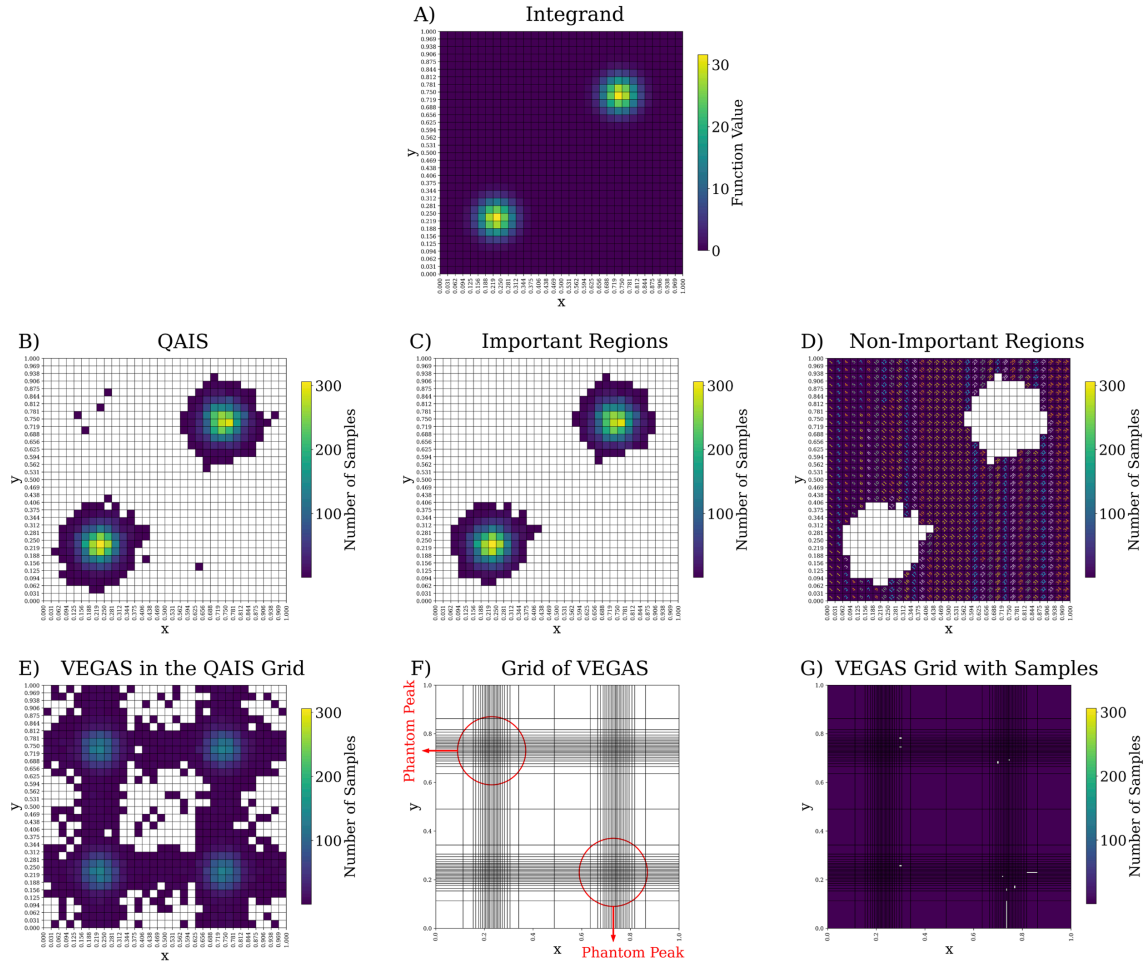


Figure 3. (A) Integrand of Eq. (3.19) on the discretized integration domain; (B) Samples obtained through QAIS; (C) Regions classified as Important; (D) Non-Important Regions, subdivided into tiles. The number of each tile demonstrates its index, and the background color the number of samples; (E) VEGAS projected to the QAIS grid; (F) VEGAS on its native grid, with phantom peaks highlighted; and (G) VEGAS on its native grid, with its corresponding number of samples per grid cell. For all cases, the number of samples used is $N = 10^4$.

the number of samples directly into the amplitude of the PQC, providing a natural mechanism for sampling, while VEGAS employs a uniform PDF over an adapted grid. Then, its grid management routine effectively shifts samples around rather than sampling from complex high-dimensional distributions. Nevertheless, sampling from a non-trivial high-dimensional PDFs would in many cases be computationally intensive with classical methods.

Furthermore, the PQC demonstrates an impressive capability to accurately capture the function's details without throwing excessive samples in less relevant regions. Additionally,

Distribution of Integration Results by Number Shots

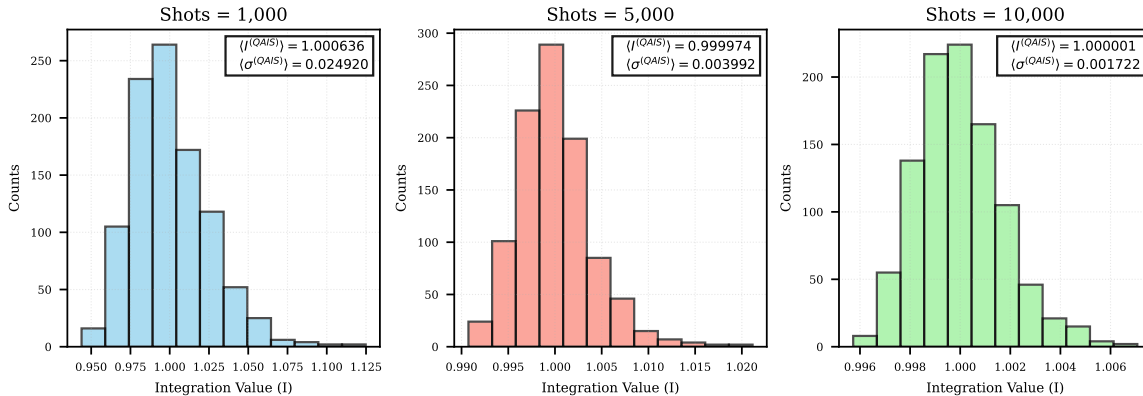


Figure 4. Integral estimations from 1000 independent runs using the same proposal PDF for the two-dimensional Gaussian integral in Eq. (3.19), as a function of the number of shots.

the Tilling algorithm is applied to separate the Important and non-Important Regions, generating an approximately monochromatic grid, which only appears in the non-Important areas. The main advantage of QAIS, as illustrated in Fig. 3, is the absence of phantom peaks. In VEGAS, this is a consequence of separability resulting in a significant number of samples being wasted in irrelevant regions and considerably reducing the performance of the algorithm. It is relevant to mention that the smallest cell size produced by VEGAS in Fig. 3 corresponds approximately to a discretization using seven qubits per dimension. Consequently, the VEGAS resolution is easily manageable with a PQC.

To demonstrate that QAIS is unbiased, we conducted a series of nested MC experiments. Because the integral is analytically normalized to 1, this exact value serves as the ground truth for validating our numerical estimates. For each experiment, we performed 1000 independent integration runs, each with a fixed proposal PDF from the same trained PQC. We then repeated these experiments with different shot counts: 1000, 5000 and 10000 samples. The results are shown in Fig. 4. We see that the average integral value oscillates around the true value, improving accuracy progressively, and does not exhibit a systematic preference toward over or underestimation when the number of samples is varied. Additionally, the average QAIS standard deviation is presented. It shall be noted that estimates that deviate significantly from the mean integral value, always exhibit inflated standard deviation. Thus, QAIS produced stable accurate and unbiased estimates without the need to sample all 2^n possible states.

Finally, we present a two-dimensional test case whose ring-shaped structure lies entirely

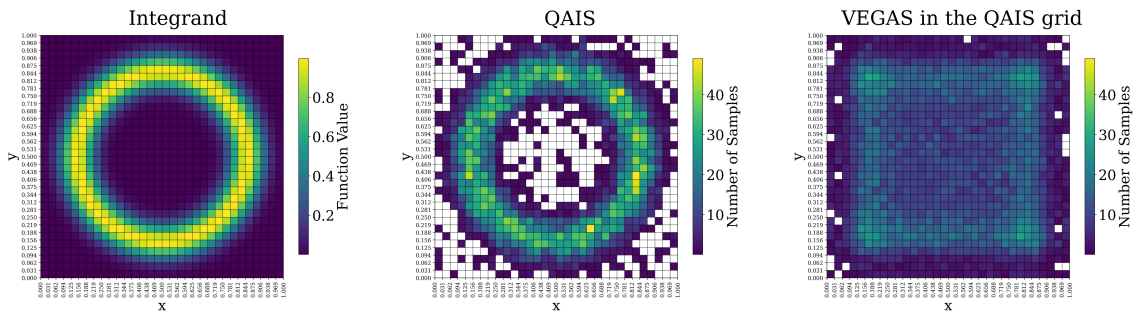


Figure 5. Comparison of VEGAS and QAIS by sample allocation for a ring-shaped integrand. The total number of samples is 10^4 .

outside VEGAS’s adaptive reach. The integral in closed form is given by

$$\int_{[0,0]}^{[1,1]} f(\mathbf{x}) d\mathbf{x} = \int_{[0,0]}^{[1,1]} e^{-200(|\mathbf{x}-\mathbf{r}|-0.35)^2} d\mathbf{x}, \quad (3.20)$$

where $\mathbf{r} = (0.5, 0.5)$. Figure 5 illustrates the results for both methods. The exponential factor puts almost the entire weight of the integrand on a thin ring of radius 0.35 centered at \mathbf{r} , while in the rest of the integration domain, it is exponentially suppressed and effectively negligible.

When VEGAS adapts the grid using the separable proposal of Eq. (2.11), it projects this PDF onto the coordinate axes, where the axis-wise viewpoint compresses the ring into two wide stripes, one in x and one in y . As a result, VEGAS distributes its samples nearly uniformly across almost all of the domain. This leads to an overwhelming number of samples landing in the empty interior and exterior of the ring, with the highest local concentrations appearing in the four corners of the square, where the integrand is negligible. On the contrary, QAIS captures in great detail the shape of the target distribution, and concentrates the samples precisely in the Important Region. This experiment illustrates how the projection based adaptation can fail when the integrand’s essential structure lies in correlations between integration variables, which motivates even further our approach of sampling from quantum states, which can naturally and efficiently encode such correlations through entanglement between registers.

4 Application of QAIS to Multi-Dimensional Integrals

In this section we apply QAIS on a set of illustrating multi-dimensional examples. First, we consider a one-loop Feynman integral with a single, very sharp peak. By construction this example highlights the strengths of MC integration and AIS, since smoothness is not a prerequisite. This is because the narrow peak must be adequately located and precisely sampled, to achieve a reliable and accurate estimate with a reasonable number of function

evaluations. In addition, this is an illustrating example to quantify how many computational basis states, out of the total exponential number of possible states, we must collect to capture with sufficient detail the most singular structures of the target function. We explicitly probe the same integrand for different number of qubits used in discretization. In this context, we expect to get reliable and robust integral estimates within a reasonable amount of shots, and without gaining significant computational overhead due to the classical post-processing coming from the number of different basis states measured.

Next, we apply QAIS to integrals containing multiple sharp localized peaks, where we expect the non-separable proposal’s strengths to appear. We consider test cases in which the underlying integrand structure consistently features the same set of peaks, although in a different number of dimensions. This setup lets us to examine how increasing the dimension of the integration space affects the quality of the learned proposal PDF, and thus its ability to capture the integrand’s correlations, and how the resulting integration uncertainty scales.

Finally, we should discuss how to extract meaningful insights from comparisons with VEGAS. Based on Eq. (2.15), VEGAS forms its final estimate, as given by combining information gathered from every proposal grid across all iterations, assigning a greater weight to more accurate iterations. A full-scale direct comparison would require from our method, not only a better final proposal PDF but also an optimization routine that remains competitive with VEGAS. However, as discussed briefly in Sec. 3.4, such a competitive process, especially for general purpose Ansätze, is still an open problem in QML. Thus, even though we have trained our PQC and obtained high quality proposal PDFs, we cannot claim an optimization procedure that can run competitively with VEGAS optimization. Therefore, we treat the trained PQC as a state preparation, where the PDF of the highly entangled quantum state gives us a very accurate sampling allocation within the exponential sized space. We then compare that one QAIS grid with the best grid VEGAS can produce. Thus, our main goal is to investigate whether a stable-sized PQC captures the intricate structures of the integrand and remain effective as the integration space grows. Additionally, we also aim to test whether and under which circumstances, the non-separable proposal PDF can outperform VEGAS’s separable one, quantify the difference, and determine if it can either reach a target accuracy with fewer samples or achieve a more precise estimate within a fixed sample budget.

4.1 One-loop pentagon Feynman integral in the Loop-Tree Duality

We consider the following one-loop scalar pentagon integral (see Fig. 6),

$$\mathcal{A}_5^{(1)}(\{p_i, m_i\}_{i=1}^5) = \int_{\ell} \prod_{i=1}^5 G_F(q_i) , \quad (4.1)$$

where $G_F(q_i) = (q_i^2 - m_i^2 + i0)^{-1}$ are Feynman propagators with mass m_i and four-momenta $q_i = \ell + \sum_{j=1}^i p_j$, with $q_5 = \ell$ by momentum conservation. The integration measure is $\int_{\ell} = -i \int d^4\ell / (2\pi)^4$, where ℓ is the loop four-momentum. The external four-momenta are p_j .

For the numerical implementation, we use the Loop-Tree Duality [67–77]. This representation is advantageous because the dimension of the integration domain is independent of

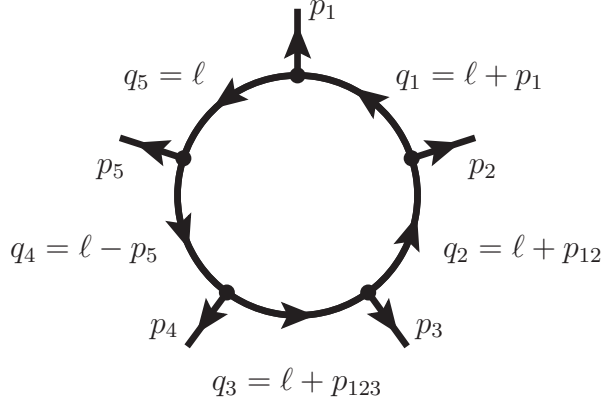


Figure 6. Pentagon Feynman diagram at one loop.

the number of external particles, specifically, it is the three-dimensional Euclidean space of the loop three-momenta. The LTD representation is obtained by analytically integrating the energy component of the loop momentum by applying the Cauchy Residue Theorem. The resulting expression is also convenient because it is manifestly causal [78–90], and so noncausal singularities of the integrand that lead to numerical instabilities are absent. In particular, the LTD representation of the one-loop scalar pentagon in Eq. (4.1), is given by

$$\mathcal{A}_5^{(1)}(\{p_i, m_i\}_{i=1}^5) = \int_{\boldsymbol{\ell}} \frac{1}{x_5} \sum \left(L_{ij}^+ L_{kl}^- + L_{ij}^- L_{kl}^+ \right), \quad \int_{\boldsymbol{\ell}} = \int_{\boldsymbol{\ell}} \frac{d^3 \boldsymbol{\ell}}{(2\pi)^3}, \quad (4.2)$$

where $x_5 = \prod_{i=1}^5 2q_{i,0}^{(+)}$ with $q_{i,0}^{(+)} = \sqrt{\mathbf{q}_i^2 + m_i^2 - i0}$ the on-shell energies of the internal particles, and

$$L_{ij}^{\pm} = \left(\frac{1}{\lambda_i^{\pm}} + \frac{1}{\lambda_j^{\pm}} \right) \frac{1}{\lambda_{ij}^{\pm}}, \quad (4.3)$$

where the causal denominators are defined as

$$\begin{aligned} \lambda_i^{\pm} &= q_{i,0}^{(+)} + q_{i+1,0}^{(+)} \pm p_{i,0}, \\ \lambda_{ij}^{\pm} &= q_{i,0}^{(+)} + q_{j+1,0}^{(+)} \pm (p_i + p_j)_0, \quad j = i + 1, \\ \lambda_{ij}^{\pm} &= \lambda_i^{\pm} + \lambda_j^{\pm}, \quad j = i + 2. \end{aligned} \quad (4.4)$$

It is understood that the indices of the on-shell energies are defined cyclically, namely $i = n + 1$ with $n = 5$ is equivalent to $i = 1$. The integrand in Eq. (4.2) depends on three independent integration variables. The loop momentum is parametrized in terms of the polar and azimuthal angles, $\boldsymbol{\ell} = |\boldsymbol{\ell}|(\sin \theta \cos \phi, \sin \theta \sin \phi, \cos \theta)$, and the modulus of the loop three-momenta is mapped to a finite interval, $|\boldsymbol{\ell}| = z/(1 - z)$ with $z \in [0, 1]$

We consider the specific kinematic configuration P11 defined in [91] and compare our results with the numerical values obtained therein. This specific configuration corresponds

One-loop Pentagon Feynman Integral

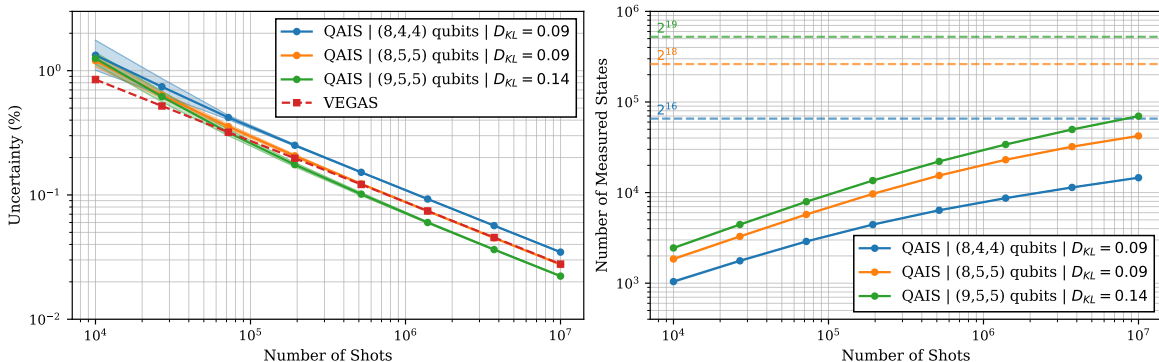


Figure 7. Average uncertainty and number of states measured for 100 independent integration runs using the same proposal PDF for the one-loop pentagon Feynman integral of Fig. 6, across the full standard MC sampling range. Each curve corresponds to a different discretization (16-19 qubits), with a proposal PDF optimized for that encoding. The shaded areas, correspond to the $\pm 1\sigma$ dispersion of these 100 runs. The VEGAS result presented corresponds to it's best iteration.

to:

$$\begin{aligned}
 p_1 &= (33.74515, 45.72730, 31.15254, -7.47943) , \\
 p_2 &= (31.36435, -41.50734, 46.47897, 2.04203) , \\
 p_3 &= (4.59005, 17.07010, 32.65403, 41.93628) , \\
 p_4 &= (29.51054, -28.25963, 46.17333, -35.08918) , \\
 m_1 &= m_2 = m_3 = m_4 = m_5 = 5.01213 .
 \end{aligned} \tag{4.5}$$

The QAIS results are presented in Fig. 7 and Fig. 8. The training of the PQC was carried out with COBYLA, the PennyLane's `lightning.qubit` noiseless state-vector simulator, and different Ansatzes with different numbers of qubits per dimension. It is worth noting that, in the smallest configuration we tested, i.e. the 16 qubits distributed as (8, 4, 4) across the three dimensions and 2×10^4 iterations, the Ansatz sequence $U^{(Z)} \rightarrow U_3$ with 144 parameters reaches $D_{KL} < 0.5$ very fast and then saturates at $D_{KL} \approx 0.27$. The results presented in Fig. 7 are obtained using the Ansatz $U^{(Z)} \rightarrow U_3 \rightarrow U^{(X)} \rightarrow U_3$, which performed best given the constraints we imposed on the number of iterations. In this case, the number of parameters ranges from 336 to 456 for 16 to 19 qubits, respectively, and the number of iterations ranges from 2×10^4 to 3×10^4 . The D_{KL} ranged from 0.09 to 0.14.

For the HEA, with the current number of iterations for the (8, 4, 4) qubit case, we tested between 2 to 8 layers, corresponding to 96 to 384 parameters, with different random initializations. The results obtained were at least one order of magnitude larger in the KL divergence ($D_{KL} > 1$), indicating a significant discrepancy. It should be noted that the optimization that starts from a uniform superposition has initial $D_{KL} \approx 6.2$.

Histograms of Integral Values | Pentagon Feynman Diagram | $9 \times 5 \times 5$ qubits

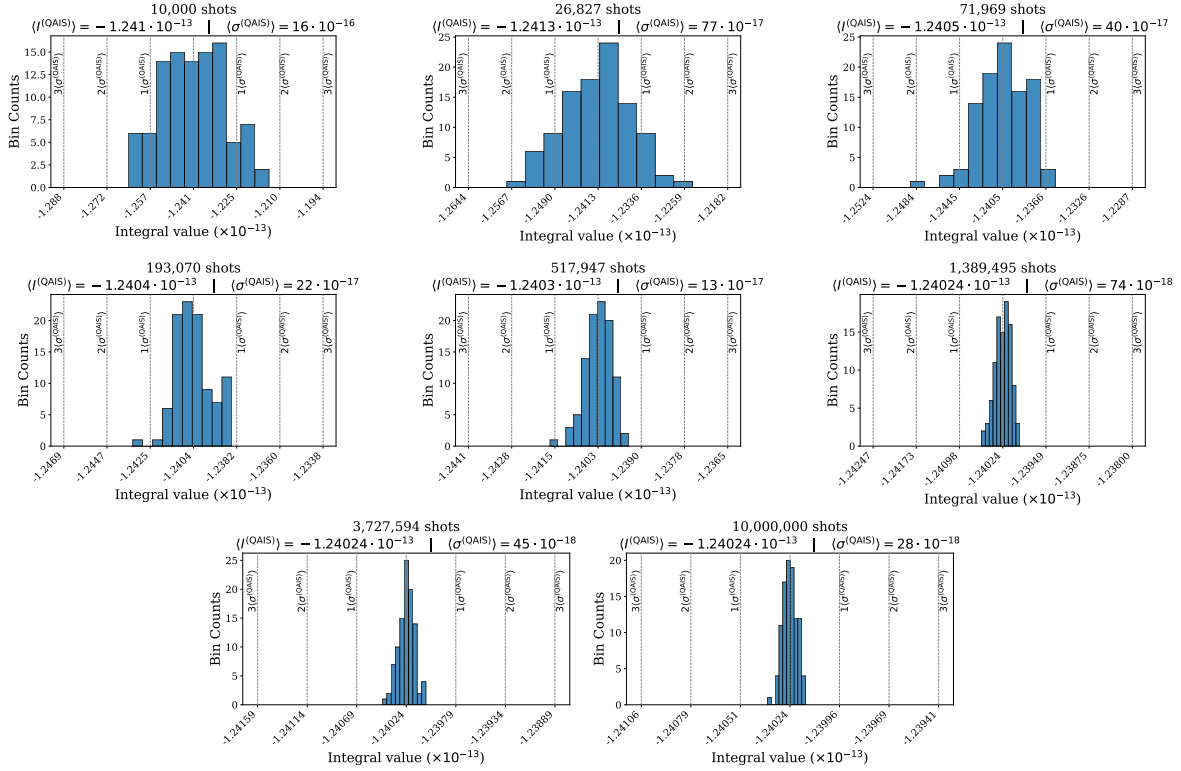


Figure 8. Histograms of the values of the 100 independent integration runs for the one-loop pentagon Feynman diagram with parameters in Eq. (4.5). The dashed vertical lines, correspond to 1σ , 2σ , and 3σ standard deviations. The reference value comes by the comparison with the classical numerical integration [91] using VEGAS, $I = -1.24027(16) \cdot 10^{-13}$.

In Fig. 7 (left), we analyze the uncertainty of the integral estimate, defined as the ratio of the standard deviation divided by the integral estimate (σ/I), as a function of the number of shots. Across all shot counts, QAIS remains competitive with VEGAS, especially with increased discretization resolutions, although the overall performance difference of the two approaches is small across the entire shot count domain.

The Fig. 7 (right) shows the amount of quantum states observed from Z -basis measurements, out of the full Hilbert space, as a function of the number of shots. We observe a controlled gradual increase as shot counts rises. Since our integrands are typically nonzero everywhere and training is inherently imperfect, the number of contributing states naturally approaches the full Hilbert space dimension 2^n asymptotically.

Nevertheless, the measurements populate only a small percentage of the Hilbert space, both in the sub-percent uncertainty region and at asymptotically large shot counts. High

accuracy therefore arises from sampling only a modest fraction of the available basis states. As the discretization is refined, that sampled fraction becomes even smaller relative to the enlarged Hilbert space, yet the quality of the estimate remains stable and improves slightly, underscoring the efficiency of direct sampling. Additional shots mainly revisit high impact cells, that have already been identified, rather than diffusing across the entire space, showing that the trained PQC focuses on refining the IS weights where the integrand is most relevant and can achieve precision without exhaustive Hilbert-space coverage.

Finally, the full integration results, run by run are presented in Fig. 8. As the sample size increases the individual estimates cluster more tightly and do not exceed one standard deviation, suggesting that our variance estimator is conservative. This behavior is expected because quasi-random sequences achieve a Root Mean Square Error that asymptotically decays faster than the $N^{-1/2}$ rate of pseudo-random MC. For quasi-random sequences, in the worst case the error is $\mathcal{O}(N^{-1}(\log N)^d)$ [92]. However, because VEGAS, whose variance is given by Eq. (2.13), serves as our reference, we report and use the conservative variance defined in Eq. (3.13).

4.2 Multi-peak Benchmark Integrals

Finally, we turn our attention to integrands with multiple peaks. This is the main part where we expect the quantum-generated PDF to surpass VEGAS’s optimal grid in a considerable and scalable way, given that the phantom peaks problem intensifies as the number of integration dimensions rises. In order to demonstrate QAIS, we have chosen the benchmark integral from the VEGAS+ study [3]. This benchmark integral contains three peaks along the diagonal. Because the projected shadows of the peaks do not cover one another in any dimension, it offers the most illustrative example of the phantom peaks problem. The analytic formula is:

$$\int_{[0,1]^d} f(\mathbf{x}) d\mathbf{x} = \int_{[0,1]^d} \left(\sum_{i=0}^d e^{-50|\mathbf{x}-\mathbf{r}_i|} \right) d\mathbf{x} \quad (4.6)$$

where $\mathbf{r}_0 = (0.23, \dots, 0.23)$, $\mathbf{r}_1 = (0.39, \dots, 0.39)$, and $\mathbf{r}_2 = (0.74, \dots, 0.74)$. We consider the cases $d = 2, 3, 4$, using the same discretization in all instances, which is five qubits per dimension. For the optimization, we employed 20×10^3 to 85×10^3 iterations for the PQC with 225-750 parameters. The Ansatz chosen is the sequence $U^{(Z)} \rightarrow U_3 \rightarrow U^{(Y)} \rightarrow U_3 \rightarrow U^{(X)} \rightarrow U_3$, which proved to be the best choice while considering the final KL divergence and the number of iterations. The resulting KL divergences fall in the range 0.09 – 0.21.

For generating the results, we made multiple identical integration runs and report the average uncertainty. It shall be noted that we observed a rare effect in the four-dimensional case, which we attribute to insufficient coverage of the Important Region and the imperfect training. In these rare runs, the variance would be getting considerably inflated. This was a consequence of not adequate sampling of one of the peaks in the extended boundary region. Thus, a large tile would be generated and evaluated with a single sample, which could fall to a badly covered part in proximity to the Important Region. To counteract this effect,

Cross-Dimensional Integration Comparison

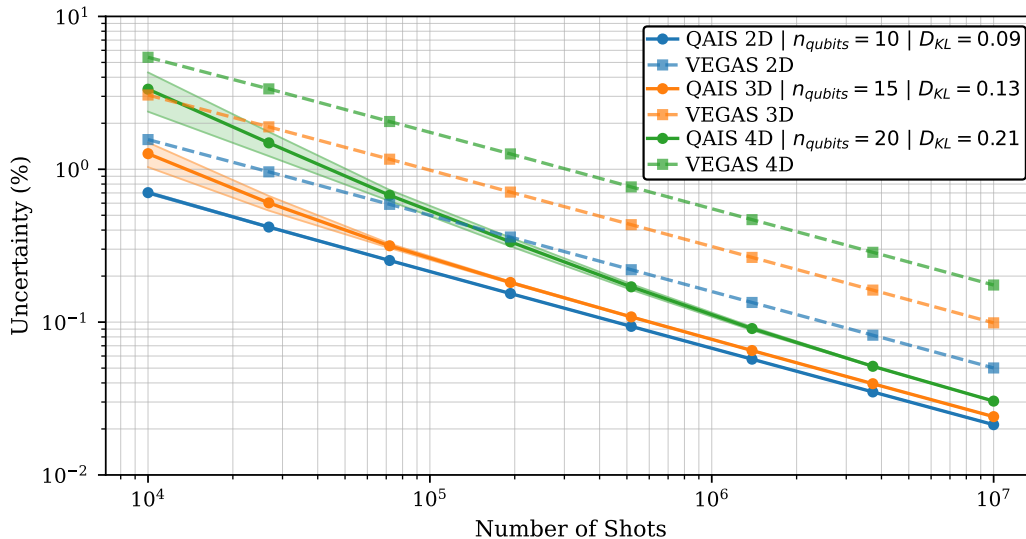


Figure 9. Average uncertainty for 100 independent integration runs using the same proposal PDF for the benchmark integral in Eq. (4.6), across the full standard MC sampling range. The shaded areas, correspond to the $\pm 1\sigma$ dispersion of these 100 runs. The VEGAS result presented corresponds to its best iteration.

we use a defensive IS mixture, to stabilize such a behavior, a strategy that is considered unbiased [93]. The mixture we have used is to sample 90% of the points from the quantum-generated proposal PDF, and the remaining 10% from a uniform PDF that are distributed in the grid after the QAIS proposal has generated it.

Figure 9 illustrates the results, where we compare QAIS with VEGAS at two-, three- and four-dimensional integrals in the form given by Eq. (4.6), across the full sampling range usually examined in MC integration. The main observation is that every QAIS curve stays well below its VEGAS counterpart over the entire range of sample budgets considered, demonstrating a robust accuracy gain that persists regardless of the dimensionality or the sample budget.

Another observation is that QAIS exhibits an increase on the uncertainty at roughly between 10^4 to 10^5 shots. The effect is clearest in the four and three-dimensional curves. This occurs because, in this budget range, the proposal PDF has still not covered and is still discovering thin boundary layers around the Important Region, in which the integrand is very small, but not totally exponentially vanishing. Thus, some regions are wrongly categorized in the non-Important Region and generate weights that do not reflect their actual contribution.

To understand this effect, it is crucial to note that if we omit the debiasing step and retain the underestimated value with its corresponding standard deviation, the resulting uncertainty curves would be as flat as those of VEGAS. Nonetheless, the modest rise in uncertainty is a small price for obtaining unbiased results. Especially while considering that the extra

uncertainty becomes insignificant above 10^5 shots. If sub-percent precision were needed at smaller budgets, a refined tiling scheme that allocates extra samples to the boundary zones could suppress this effect without compromising unbiasedness.

On the overall cross-dimensional performance, based on our observations from Fig. 9, the decisive metric is the KL divergence. The two and three-dimensional proposals have divergences that are very close and their uncertainty difference is negligible above 10^5 shots. This behavior aligns with our expectations, according to the form of the IS variance in Eq. (3.13), since the statistical error is governed by the proposal PDF’s quality rather than by the dimension of the integral. In the four-dimensional case, the best proposal we could train to had a comparatively larger divergence ($D_{KL} \approx 0.21$), shifting its uncertainty curve upwards. Nevertheless, it was able to reach the accuracy and surpass the two-dimensional VEGAS case in the sub-percentage accuracy region, hinting that even a non-perfect KL divergence can generate precise results. Ultimately, in the asymptotic region it nearly matches the precision of the other two curves.

Finally, to motivate the general scaling to higher dimensions, it is important to note that for a number of non-mutually covered peaks p , the number of phantom peaks is $p^d - p$. Then, only the fraction p/p^d of all samples reaches the true peaks, the MC standard deviation grows as $\sigma \propto p^{\frac{d-1}{2}}/\sqrt{N}$. Consequently, if a quantum-generated proposal PDF keeps the KL divergence low with a computationally competitive state preparation, even as the number of dimension grows, it will reduce the sample budget needed for a given precision in a scalable way and thus achieve significant improvements in accuracy.

5 Conclusions and Outlook

We have presented a novel Monte Carlo integration method that performs Adaptive Importance Sampling (AIS) using a Parametrized Quantum Circuit (PQC). Inspired by the success of classical AIS integrators, such as VEGAS, we aim to address their limitations and identified the two main directions in which quantum computing can contribute.

Firstly, the standard approach to numerical integration using AIS involves discretizing the integration domain into a multidimensional grid. The grid’s size grows exponentially with the number of dimensions, and manipulating a Probability Density Function (PDF) in the integration domain through such a grid soon becomes computationally prohibitive. To overcome these drawbacks, we encode the grid directly in an n -qubit Hilbert space and manipulate the PDF via a strongly entangled Parameterized Quantum Circuit (PQC). We employ generative modeling to train and obtain an optimal PQC whose PDF accurately reflects the underlying structure of the target integrand.

Second, although Importance Sampling is an exceptionally effective variance reduction framework, its performance depends critically on the proposal PDF. By shaping this probability distribution with a highly expressive entangled PQC, we efficiently sample from complex non-separable PDFs that capture directly all of the correlations in the multidimensional space. This strategy enhances the performance of Importance Sampling.

For the demonstration of the performance of the method, we applied QAIS to integrate two challenging types of functions and compared the results with VEGAS, which serves as our reference. These functions are a sharply-peaked single-mode one-loop Feynman integrand, and a set of multi-modal benchmark integrands from two to four dimensions. For the first case, the two methods performed comparably overall. For the multi-modal functions, VEGAS allocated a substantial amount of samples in non-Important Regions, especially as the dimension increased, due to its separable proposal PDF, whereas QAIS consistently maintained impressive accuracy.

As a future work, we intend to make our integration workflow more competitive by refining the current optimization procedure. While QAIS already represents richer PDFs, a reliable optimization routine, especially as robust as the one of VEGAS, remains challenging, as in many current Quantum Machine Learning approaches. We therefore plan to formalize the optimization procedure in detail with more specific PQC architectures, combining them with initialization of the optimization process with easily loadable approximations of the target functions and other established heuristics.

Acknowledgements

This work is supported by the Spanish Government and ERDF/EU - Agencia Estatal de Investigación (MCIU/AEI/10.13039/501100011033), Grants No. PID2023-146220NB-I00, No. PID2020-114473GB-I00, and No. CEX2023-001292-S; and Generalitat Valenciana, Grant No. ASFAE/2022/009 (Planes Complementarios de I+D+i, NextGenerationEU). KP is supported by Grants No. CEX2023-001292-S and No. ASFAE/2022/009. JML is supported by Generalitat Valenciana, Grant No. ACIF/2021/219. This work is also supported by the Ministry of Economic Affairs and Digital Transformation of the Spanish Government and NextGenerationEU through the Quantum Spain project, and by CSIC Interdisciplinary Thematic Platform (PTI+) on Quantum Technologies (PTI-QTEP+).

A Tiling Algorithm

The tiling algorithm constructed to cover the d -dimensional space proceeds as follows. We consider a d -dimensional grid in which axis i is subdivided into 2^{q_i} uniform cells. The grid contains 2^n cells in total, with $n = \sum_{i=1}^d q_i$. Every grid cell is labeled by an n -bit string s , partitioned into the d dimensions as:

$$s = s^{(n)} \rightarrow (s^{(q_d)}, s^{(q_{d-1})}, \dots, s^{(q_1)}), \quad |s^{(q_i)}| = q_i, \quad (\text{A.1})$$

where the full bitstring's sub-block $s^{(q_i)}$ encodes the coordinate on axis i . Throughout this work we adopt BEE conventions, i.e. the left-most bit is most significant when converting s to the integer

$$\text{int}(s^{(q_i)}) \in \{0, \dots, 2^{q_i} - 1\}. \quad (\text{A.2})$$

Under this encoding the mapping

$$s \mapsto (x_d, x_{d-1}, \dots, x_1), \quad x_i \in \{0, \dots, 2^{q_i} - 1\}, \quad (\text{A.3})$$

is one-to-one between bit strings and grid cell coordinates.

After performing N measurements we obtain M distinct outcome strings, sparsely distributed within the 2^n sized space:

$$\{(s_1, p(s_1)), \dots, (s_M, p(s_M))\}, \quad (\text{A.4})$$

where each $p(s_k)$ is the empirical frequency of s_k . Sorting these strings in an ascending order costs $\mathcal{O}(M \log M)$, or $\mathcal{O}(n M \log M)$ if the comparison cost in n bits is considered also. For consecutive sorted strings $s_k < s_{k+1}$ we define the gap size :

$$\Delta_k = \text{int}(s_{k+1}) - \text{int}(s_k) - 1. \quad (\text{A.5})$$

If $\Delta_k > 0$ there are Δ_k unobserved cells strictly between s_k and s_{k+1} . If $\Delta_k = 0$ the two observed cells are adjacent. Then, we proceed with the greedy construction of the hyper-rectangles to cover the missing ranges. The main difficulty is to cover every gap with a few hyper-rectangles, depending only on d and n and the number of measured outcomes M while not depending on the exponentially large pool of unmeasured states $2^n - M = \sum_k \Delta_k$. The main procedure (lines 26-44 of Algorithm 1) expands greedily from the least-significant right-most dimension towards the most-significant left-most one, grouping whole blocks of cells whenever lower-order dimensions are already fully spanned.

Starting from the lower corner of a gap, the tiling algorithm iteratively constructs a tile that never exceeds the boundary 2^{q_i} on any axis, never exceeds the remaining gap size Δ_k , and expands the dimension $i + 1$ only after dimension i has been filled from coordinate 0 up to its boundary. In each dimension except the highest-order one, at most two separate expansions are made. The top dimension cannot have full expansions. Consequently, a single gap is covered by at most $2(d - 1) + 1$ hyper-rectangles.

Once all gaps are tiled, we obtain an ordered list of measured points and hyper-rectangles that jointly cover the entire space. Collapsing the unmeasured tiles into the non-Important Region (as described in Sec. 3.3) is now straightforward. Each empty tile is merged with the next measured state, the latter's probability $p(s_{k+1})$ being assigned to the entire hyper-rectangle. If necessary, for the last interval, (from s_M to the binary state $11 \dots 11$), we generate an additional tile, and merge it into the group containing s_M . Because the associated list is compact and sorted, alternative ways of performing the de-biasing are possible. For example, merging neighboring tiles with common boundaries.

Nevertheless, in this work, we follow the simplest approach for the sake of clarity, simplicity and to serve as a proof of concept, with the potential for adaptation. The full pseudocode, including complexity hints for every operation, is given in Alg. 1.

Algorithm 1 Tiling Algorithm for Multi-Dimensional Spaces

```

1: Input:   • Grid dimensions:  $grid\_dims = [2^{q_d}, \dots, 2^{q_1}]$ 
2:           • Dictionary of Measured States as Bitstrings and Probabilities:  $S$ 
3: Output: Dictionary, with tiles (in coordinate format), that cover the integration space.
=====
4: Initialize Result Dictionary (Associated Array):  $F \leftarrow \{\}$ 
5: Sort the states:  $S \leftarrow \{(s_1, p(s_1)), (s_2, p(s_2)), \dots, (s_M, p(s_M))\}$  ▷  $\mathcal{O}(M \log M)$ 
6: for  $i \leftarrow 1$  to  $M - 1$  do ▷  $\mathcal{O}(M)$ 
7:    $\Delta \leftarrow \text{int}(s_{i+1}) - \text{int}(s_i) - 1$  ▷ Cells to fill
8:   if  $\Delta > 0$  then
9:      $current\_linear \leftarrow \text{int}(s_i) + 1$ 
10:     $tile\_intervals \leftarrow \text{INTERVALSGENERATOR}(grid\_dims, current\_linear, \Delta)$  ▷  $\mathcal{O}(d^3 n^2)$ 
11:    Append  $(tile\_intervals, 0)$  to  $F$ 
12:  else if  $\Delta = 0$  then
13:     $end\_coord \leftarrow current\_coord$ 
14:    Append  $((current\_coord, end\_coord), p(s_i))$  to  $F$ 
15:  end if
16: end for
17: return  $F$ 
=====
18: procedure  $\text{INTERVALSGENERATOR}(grid\_dims, current\_linear, \Delta)$ 
19:   Initialize:  $intervals \leftarrow \emptyset$ 
20:   while  $\Delta > 0$  do ▷ # of loops bounded by:  $|intervals| \approx \mathcal{O}(d)$ 
21:      $current\_coord \leftarrow \text{lin\_to\_coord}(current\_linear)$  ▷ Int. to grid coord. (BEE)
22:      $(tile\_shape, cells\_filled) \leftarrow \text{GREEDYMULTIDIMEXPAND}(current\_coord, \Delta)$ 
23:      $end\_coord \leftarrow (current\_coord[i] + tile\_shape[i] - 1), \quad i = 1, \dots, d$ 
24:     Append  $(current\_coord, end\_coord)$  to  $intervals$ 
25:      $\Delta \leftarrow \Delta - cells\_filled$ 
26:      $current\_linear \leftarrow current\_linear + cells\_filled$ 
27:   end while
28:   return  $intervals$  ▷  $|intervals| \leq 2 * (d - 1) + 1$ 
29: end procedure
=====
30: procedure  $\text{GREEDYMULTIDIMEXPAND}(current\_coord, \Delta)$ 
31:   Initialize:  $tile\_shape \leftarrow [1, \dots, 1]$  ▷  $|tile\_shape| = d$ 
32:    $tile\_shape[d] \leftarrow \min\{\Delta, grid\_dims[d] - current\_coord[d]\}$ 
33:   for  $i \leftarrow d - 1$  down to  $1$  do ▷  $\mathcal{O}(d)$ 
34:     if  $current\_coord[i + 1] = 0$  and  $tile\_shape[i + 1] = grid\_dims[i + 1]$  then
35:        $comb\_vol \leftarrow \prod_{j=i+1}^d grid\_dims[j]$  ▷  $\mathcal{O}(d n^2)$ 
36:        $tile\_extend \leftarrow \lfloor \Delta / comb\_vol \rfloor$ 
37:       if  $tile\_extend > 0$  then
38:          $tile\_shape[i] \leftarrow \min\{grid\_dims[i] - current\_coord[i], tile\_extend\}$ 
39:       else
40:          $tile\_shape[i] \leftarrow 1$ 
41:       end if
42:     else
43:        $tile\_shape[i] \leftarrow 1$ 
44:     end if
45:   end for
46:    $block\_vol \leftarrow \prod_{i=1}^d tile\_shape[i]$ 
47:   return  $(tile\_shape, block\_vol)$ 
48: end procedure
=====

```

References

- [1] G. P. Lepage, *A New Algorithm for Adaptive Multidimensional Integration*, *J. Comput. Phys.* **27** (1978) 192.
- [2] G. P. Lepage, *VEGAS - an adaptive multi-dimensional integration program*, tech. rep., Cornell Univ. Lab. Nucl. Stud., Ithaca, NY, 1980.
- [3] G. P. Lepage, *Adaptive multidimensional integration: VEGAS enhanced*, *J. Comput. Phys.* **439** (2021) 110386, [[2009.05112](#)].
- [4] T. Hahn, *CUBA: A Library for multidimensional numerical integration*, *Comput. Phys. Commun.* **168** (2005) 78–95, [[hep-ph/0404043](#)].
- [5] J. Alwall, M. Herquet, F. Maltoni, O. Mattelaer and T. Stelzer, *MadGraph 5 : Going Beyond*, *JHEP* **06** (2011) 128, [[1106.0522](#)].
- [6] T. Gleisberg, S. Hoeche, F. Krauss, M. Schonherr, S. Schumann, F. Siegert et al., *Event generation with SHERPA 1.1*, *JHEP* **02** (2009) 007, [[0811.4622](#)].
- [7] E. Bothmann, T. Janßen, M. Knobbe, T. Schmale and S. Schumann, *Exploring phase space with Neural Importance Sampling*, *SciPost Phys.* **8** (2020) 069, [[2001.05478](#)].
- [8] R. Winterhalder, V. Magerya, E. Villa, S. P. Jones, M. Kerner, A. Butter et al., *Targeting multi-loop integrals with neural networks*, *SciPost Phys.* **12** (2022) 129, [[2112.09145](#)].
- [9] S. Carrazza and J. M. Cruz-Martinez, *VegasFlow: accelerating Monte Carlo simulation across multiple hardware platforms*, *Comput. Phys. Commun.* **254** (2020) 107376, [[2002.12921](#)].
- [10] P. W. Shor, *Polynomial-time algorithms for prime factorization and discrete logarithms on a quantum computer*, *SIAM Journal on Computing* **26** (Oct., 1997) 1484–1509.
- [11] L. K. Grover, *A fast quantum mechanical algorithm for database search*, 1996.
- [12] A. W. Harrow, A. Hassidim and S. Lloyd, *Quantum algorithm for linear systems of equations*, *Physical Review Letters* **103** (Oct., 2009) .
- [13] J. J. M. de Lejarza, M. Grossi, L. Cieri and G. Rodrigo, *Quantum Fourier Iterative Amplitude Estimation*, in *2023 International Conference on Quantum Computing and Engineering*, IEEE, 5, 2023. [2305.01686](#). DOI.
- [14] J. J. M. de Lejarza, L. Cieri, M. Grossi, S. Vallecorsa and G. Rodrigo, *Loop Feynman integration on a quantum computer*, *Phys. Rev. D* **110** (2024) 074031, [[2401.03023](#)].
- [15] J. J. M. de Lejarza, D. F. Rentería-Estrada, M. Grossi and G. Rodrigo, *Quantum integration of decay rates at second order in perturbation theory*, *Quantum Sci. Technol.* **10** (2025) 025026, [[2409.12236](#)].
- [16] G. Rodrigo, *Quantum Algorithms in Particle Physics*, *Acta Phys. Polon. Supp.* **17** (2024) 2–A14, [[2401.16208](#)].
- [17] G. Agliardi, M. Grossi, M. Pellen and E. Prati, *Quantum integration of elementary particle processes*, *Phys. Lett. B* **832** (2022) 137228, [[2201.01547](#)].
- [18] I. Williams and M. Pellen, *A general approach to quantum integration of cross sections in high-energy physics*, [2502.14647](#).

- [19] J. M. Cruz-Martinez, M. Robbiati and S. Carrazza, *Multi-variable integration with a variational quantum circuit*, *Quantum Sci. Technol.* **9** (2024) 035053, [2308.05657].
- [20] G. Brassard, P. Høyer, M. Mosca and A. Tapp, *Quantum amplitude amplification and estimation*, 2002. 10.1090/conm/305/05215.
- [21] A. Montanaro, *Quantum speedup of monte carlo methods*, *Proceedings of the Royal Society A: Mathematical, Physical and Engineering Sciences* **471** (Sept., 2015) 20150301.
- [22] F. Arute et al., *Quantum supremacy using a programmable superconducting processor*, *Nature* **574** (2019) 505–510, [1910.11333].
- [23] J. Romero and A. Aspuru-Guzik, *Variational quantum generators: Generative adversarial quantum machine learning for continuous distributions*, *Advanced Quantum Technologies* **4** (2021) 2000003.
- [24] A. E. Paine, V. E. Elfving and O. Kyriienko, *Quantum quantile mechanics: Solving stochastic differential equations for generating time-series*, *Advanced Quantum Technologies* **6** (Aug, 2023) 2300065.
- [25] E. Y. Zhu, S. Johri, D. Bacon, M. Esencan, J. Kim, M. Muir et al., *Generative quantum learning of joint probability distribution functions*, *Phys. Rev. Res.* **4** (Nov, 2022) 043092.
- [26] O. Kyriienko, A. E. Paine and V. E. Elfving, *Protocols for trainable and differentiable quantum generative modeling*, *Phys. Rev. Res.* **6** (Sep, 2024) 033291.
- [27] S. Kasture, O. Kyriienko and V. E. Elfving, *Protocols for classically training quantum generative models on probability distributions*, *Phys. Rev. A* **108** (Oct, 2023) 042406.
- [28] M. S. Rudolph, S. Lerch, S. Thanasilp, O. Kiss, S. Vallecorsa, M. Grossi et al., *Trainability barriers and opportunities in quantum generative modeling*, 2023.
- [29] S. Lloyd and C. Weedbrook, *Quantum generative adversarial learning*, *Phys. Rev. Lett.* **121** (Jul, 2018) 040502.
- [30] P.-L. Dallaire-Demers and N. Killoran, *Quantum generative adversarial networks*, *Phys. Rev. A* **98** (Jul, 2018) 012324.
- [31] C. Zoufal, A. Lucchi and S. Woerner, *Quantum generative adversarial networks for learning and loading random distributions*, *npj Quantum Information* **5** (Nov, 2019) 103.
- [32] H.-L. Huang, Y. Du, M. Gong, Y. Zhao, Y. Wu, C. Wang et al., *Experimental quantum generative adversarial networks for image generation*, *Phys. Rev. Applied* **16** (Aug, 2021) 024051.
- [33] C. Zoufal, A. Lucchi and S. Woerner, *Variational quantum boltzmann machines*, *Quantum Machine Intelligence* **3** (Feb, 2021) .
- [34] L. Coopmans and M. Benedetti, *On the sample complexity of quantum boltzmann machine learning*, *Commun. Phys.* **7** (Aug, 2024) .
- [35] J.-G. Liu and L. Wang, *Differentiable learning of quantum circuit born machines*, *Phys. Rev. A* **98** (Dec, 2018) 062324.
- [36] M. Benedetti, D. Garcia-Pintos, O. Perdomo, V. Leyton-Ortega, Y. Nam and A. Perdomo-Ortiz, *A generative modeling approach for benchmarking and training shallow quantum circuits*, *npj Quantum Information* **5** (May, 2019) 45.

- [37] M. Benedetti, E. Lloyd, S. Sack and M. Fiorentini, *Erratum: Parameterized quantum circuits as machine learning models (2019 quant. sci. tech. 4 043001)*, *Quantum Science and Technology* **5** (dec, 2019) 019601.
- [38] O. Kiss, M. Grossi, E. Kajomovitz and S. Vallecorsa, *Conditional born machine for monte carlo event generation*, *Phys. Rev. A* **106** (Aug, 2022) 022612.
- [39] M. Hibat-Allah, M. Mauri, J. Carrasquilla and A. Perdomo-Ortiz, *A framework for demonstrating practical quantum advantage: comparing quantum against classical generative models*, *Communications Physics* **7** (2024) 68.
- [40] A. Delgado et al., *Quantum Computing for Data Analysis in High-Energy Physics*, in *Snowmass 2021*, 3, 2022. [2203.08805](#).
- [41] A. Delgado, F. Rios and K. E. Hamilton, *Identifying overparameterization in Quantum Circuit Born Machines*, [2307.03292](#).
- [42] A. Delgado, D. Venegas-Vargas, A. Huynh and K. Carroll, *Towards Designing Scalable Quantum-Enhanced Generative Networks for Neutrino Physics Experiments with Liquid Argon Time Projection Chambers*, [2410.12650](#).
- [43] E. Bermot, C. Zoufal, M. Grossi, J. Schuhmacher, F. Tacchino, S. Vallecorsa et al., *Quantum generative adversarial networks for anomaly detection in high energy physics*, in *2023 IEEE International Conference on Quantum Computing and Engineering (QCE)*, vol. 01, pp. 331–341, 2023. [DOI](#).
- [44] C. Tüysüz, M. Demidik, L. Coopmans, E. Rinaldi, V. Croft, Y. Haddad et al., *Learning to generate high-dimensional distributions with low-dimensional quantum Boltzmann machines*, [2410.16363](#).
- [45] M. S. Rudolph, S. Lerch, S. Thanasilp, O. Kiss, O. Shaya, S. Vallecorsa et al., *Trainability barriers and opportunities in quantum generative modeling*, *npj Quantum Inf.* **10** (2024) 116, [[2305.02881](#)].
- [46] J. J. M. de Lejarza, H.-Y. Wu, O. Kyriienko, G. Rodrigo and M. Grossi, *Quantum Chebyshev Probabilistic Models for Fragmentation Functions*, [2503.16073](#).
- [47] J. J. Martínez de Lejarza, L. Cieri and G. Rodrigo, *Quantum clustering and jet reconstruction at the lhc*, *Phys. Rev. D* **106** (Aug, 2022) 036021.
- [48] J. J. M. de Lejarza, L. Cieri and G. Rodrigo, *Quantum jet clustering with LHC simulated data*, *PoS ICHEP2022* (2022) 241, [[2209.08914](#)].
- [49] V. Belis, K. A. Woźniak, E. Puljak, P. Barkoutsos, G. Dissertori, M. Grossi et al., *Quantum anomaly detection in the latent space of proton collision events at the LHC*, *Commun. Phys.* **7** (2024) 334, [[2301.10780](#)].
- [50] J. Schuhmacher, L. Boggia, V. Belis, E. Puljak, M. Grossi, M. Pierini et al., *Unravelling physics beyond the standard model with classical and quantum anomaly detection*, *Machine Learning: Science and Technology* **4** (nov, 2023) 045031.
- [51] V. Belis, P. Odagiu, M. Grossi, F. Reiter, G. Dissertori and S. Vallecorsa, *Guided quantum compression for high dimensional data classification*, *Mach. Learn. Sci. Tech.* **5** (2024) 035010, [[2402.09524](#)].

- [52] V. Belis, S. González-Castillo, C. Reissel, S. Vallecorsa, E. F. Combarro, G. Dissertori et al., *Higgs analysis with quantum classifiers*, *EPJ Web Conf.* **251** (2021) 03070, [[2104.07692](#)].
- [53] M. Casals, V. Belis, E. F. Combarro, E. Alarcón, S. Vallecorsa and M. Grossi, *Guided Graph Compression for Quantum Graph Neural Networks*, [2506.09862](#).
- [54] I. Sobol', *On the distribution of points in a cube and the approximate evaluation of integrals*, *USSR Computational Mathematics and Mathematical Physics* **7** (1967) 86–112.
- [55] A. Tridgell, P. Mackerras et al., *The rsync algorithm*, .
- [56] J. C. Mogul, F. Douglass, A. Feldmann and B. Krishnamurthy, *Potential benefits of delta encoding and data compression for http*, in *Proceedings of the ACM SIGCOMM '97 Conference on Applications, Technologies, Architectures, and Protocols for Computer Communication*, SIGCOMM '97, (New York, NY, USA), p. 181–194, Association for Computing Machinery, 1997. [DOI](#).
- [57] A. Sykes, “Meshing in a minecraft game.” Blog post on 0fps.net, June, 2012.
- [58] S. Kullback and R. A. Leibler, *On Information and Sufficiency*, *The Annals of Mathematical Statistics* **22** (1951) 79–86.
- [59] M. Cerezo, G. Verdon, H.-Y. Huang, L. Cincio and P. J. Coles, *Challenges and opportunities in quantum machine learning*, *Nature Computational Science* **2** (Sept., 2022) 567–576.
- [60] A. Abbas, A. Ambainis, B. Augustino, A. Bärttschi, H. Buhrman, C. Coffrin et al., *Challenges and opportunities in quantum optimization*, *Nature Reviews Physics* **6** (Oct., 2024) 718–735.
- [61] E. Fontana, D. Herman, S. Chakrabarti, N. Kumar, R. Yalovetzky, J. Heredge et al., *Characterizing barren plateaus in quantum ansätze with the adjoint representation*, *Nature Communications* **15** (Aug., 2024) .
- [62] M. Schuld, A. Bocharov, K. M. Svore and N. Wiebe, *Circuit-centric quantum classifiers*, *Physical Review A* **101** (Mar., 2020) .
- [63] L. Leone, S. F. Oliviero, L. Cincio and M. Cerezo, *On the practical usefulness of the hardware efficient ansatz*, *Quantum* **8** (July, 2024) 1395.
- [64] M. J. D. Powell, *A Direct Search Optimization Method That Models the Objective and Constraint Functions by Linear Interpolation*. 1994. [10.1007/978-94-015-8330-5_4](#).
- [65] M. J. D. Powell, *Direct search algorithms for optimization calculations*, *Acta Numerica* **7** (1998) 287–336.
- [66] D. P. Kingma and J. Ba, *Adam: A method for stochastic optimization*, 2017.
- [67] S. Catani, T. Gleisberg, F. Krauss, G. Rodrigo and J.-C. Winter, *From loops to trees by-passing Feynman’s theorem*, *JHEP* **09** (2008) 065, [[0804.3170](#)].
- [68] I. Bierenbaum, S. Catani, P. Draggiotis and G. Rodrigo, *A Tree-Loop Duality Relation at Two Loops and Beyond*, *JHEP* **10** (2010) 073, [[1007.0194](#)].
- [69] I. Bierenbaum, S. Buchta, P. Draggiotis, I. Malamos and G. Rodrigo, *Tree-Loop Duality Relation beyond simple poles*, *JHEP* **03** (2013) 025, [[1211.5048](#)].
- [70] S. Buchta, G. Chachamis, P. Draggiotis, I. Malamos and G. Rodrigo, *On the singular behaviour of scattering amplitudes in quantum field theory*, *JHEP* **11** (2014) 014, [[1405.7850](#)].

- [71] F. Driencourt-Mangin, G. Rodrigo, G. F. R. Sborlini and W. J. Torres Bobadilla, *Universal four-dimensional representation of $H \rightarrow \gamma\gamma$ at two loops through the Loop-Tree Duality*, *JHEP* **02** (2019) 143, [[1901.09853](#)].
- [72] R. Runkel, Z. Ször, J. P. Vesga and S. Weinzierl, *Causality and loop-tree duality at higher loops*, *Phys. Rev. Lett.* **122** (2019) 111603, [[1902.02135](#)].
- [73] J. J. Aguilera-Verdugo, F. Driencourt-Mangin, J. Plenter, S. Ramírez-Uribe, G. Rodrigo, G. F. R. Sborlini et al., *Causality, unitarity thresholds, anomalous thresholds and infrared singularities from the loop-tree duality at higher orders*, *JHEP* **12** (2019) 163, [[1904.08389](#)].
- [74] R. Runkel, Z. Ször, J. P. Vesga and S. Weinzierl, *Integrands of loop amplitudes within loop-tree duality*, *Phys. Rev. D* **101** (2020) 116014, [[1906.02218](#)].
- [75] Z. Capatti, V. Hirschi, D. Kermanschah and B. Ruijl, *Loop-Tree Duality for Multiloop Numerical Integration*, *Phys. Rev. Lett.* **123** (2019) 151602, [[1906.06138](#)].
- [76] Z. Capatti, V. Hirschi, D. Kermanschah, A. Pelloni and B. Ruijl, *Numerical Loop-Tree Duality: contour deformation and subtraction*, *JHEP* **04** (2020) 096, [[1912.09291](#)].
- [77] W. J. T. Bobadilla, *Lotty – The loop-tree duality automation*, *Eur. Phys. J. C* **81** (2021) 514, [[2103.09237](#)].
- [78] J. J. Aguilera-Verdugo, F. Driencourt-Mangin, R. J. Hernández-Pinto, J. Plenter, S. Ramírez-Uribe, A. E. Rentería Olivo et al., *Open Loop Amplitudes and Causality to All Orders and Powers from the Loop-Tree Duality*, *Phys. Rev. Lett.* **124** (2020) 211602, [[2001.03564](#)].
- [79] S. Ramírez-Uribe, P. K. Dhani, G. F. R. Sborlini and G. Rodrigo, *Rewording Theoretical Predictions at Colliders with Vacuum Amplitudes*, *Phys. Rev. Lett.* **133** (2024) 211901, [[2404.05491](#)].
- [80] LTD collaboration, S. Ramírez-Uribe, A. E. Rentería-Olivo, D. F. Rentería-Estrada, J. J. M. de Lejarza, P. K. Dhani, L. Cieri et al., *Vacuum amplitudes and time-like causal unitarity in the loop-tree duality*, *JHEP* **01** (2025) 103, [[2404.05492](#)].
- [81] I. L. Imaz and G. F. R. Sborlini, *Analysis of symmetries in the causal loop-tree duality representations*, *Phys. Rev. D* **111** (2025) 105016, [[2502.14179](#)].
- [82] J. Rios-Sanchez and G. Sborlini, *Toward multiloop local renormalization within causal loop-tree duality*, *Phys. Rev. D* **109** (2024) 125004, [[2402.13995](#)].
- [83] J. J. Aguilera-Verdugo, R. J. Hernandez-Pinto, G. Rodrigo, G. F. R. Sborlini and W. J. Torres Bobadilla, *Causal representation of multi-loop Feynman integrands within the loop-tree duality*, *JHEP* **01** (2021) 069, [[2006.11217](#)].
- [84] S. Ramírez-Uribe, R. J. Hernández-Pinto, G. Rodrigo, G. F. R. Sborlini and W. J. Torres Bobadilla, *Universal opening of four-loop scattering amplitudes to trees*, *JHEP* **04** (2021) 129, [[2006.13818](#)].
- [85] W. J. Torres Bobadilla, *Loop-tree duality from vertices and edges*, *JHEP* **04** (2021) 183, [[2102.05048](#)].
- [86] G. F. R. Sborlini, *Geometrical approach to causality in multiloop amplitudes*, *Phys. Rev. D* **104** (2021) 036014, [[2102.05062](#)].

- [87] S. Kromin, N. Schwanemann and S. Weinzierl, *Amplitudes within causal loop-tree duality*, *Phys. Rev. D* **106** (2022) 076006, [[2208.01060](#)].
- [88] S. Ramírez-Uribe, A. E. Rentería-Olivo, G. Rodrigo, G. F. R. Sborlini and L. Vale Silva, *Quantum algorithm for Feynman loop integrals*, *JHEP* **05** (2022) 100, [[2105.08703](#)].
- [89] G. Clemente, A. Crippa, K. Jansen, S. Ramírez-Uribe, A. E. Rentería-Olivo, G. Rodrigo et al., *Variational quantum eigensolver for causal loop Feynman diagrams and directed acyclic graphs*, *Phys. Rev. D* **108** (2023) 096035, [[2210.13240](#)].
- [90] S. Ramírez-Uribe, A. E. Rentería-Olivo and G. Rodrigo, *Quantum querying based on multicontrolled Toffoli gates for causal Feynman loop configurations and directed acyclic graphs*, [2404.03544](#).
- [91] S. Buchta, G. Chachamis, P. Draggiotis and G. Rodrigo, *Numerical implementation of the loop-tree duality method*, *Eur. Phys. J. C* **77** (2017) 274, [[1510.00187](#)].
- [92] H. Niederreiter, *Random Number Generation and Quasi-Monte Carlo Methods*. Society for Industrial and Applied Mathematics, 1992. [10.1137/1.9781611970081](#).
- [93] T. Hesterberg, *Weighted average importance sampling and defensive mixture distributions*, *Technometrics* **37** (1995) 185–194.